



SAPIENZA
UNIVERSITÀ DI ROMA

The MONDO secondary neutron tracker for particle therapy application: implementation of the event reconstruction algorithm

Facoltà di Scienze Matematiche, Fisiche e Naturali

Corso di Laurea Magistrale in Particle and Astroparticle Physics

Candidate

Antonio Trigilio

ID number 1816189

Thesis Advisor

Prof. Riccardo Faccini

Co-Advisor

Dr. Michela Marafini

Academic Year 2020/2021

The MONDO secondary neutron tracker for particle therapy application: implementation of the event reconstruction algorithm

Master's thesis. Sapienza – University of Rome

© 2020 Antonio Trigilio. All rights reserved

This thesis has been typeset by L^AT_EX and the Sapthesis class.

Author's email: trigilio.1816189@studenti.uniroma1.it

*Ai miei genitori, che mi hanno guidato nel mondo
e a Eliana, che l'ha reso un posto meraviglioso.*

It was the best of times, it was the worst of times,
it was the age of wisdom, it was the age of foolishness,
it was the epoch of belief, it was the epoch of incredulity,
it was the season of Light, it was the season of Darkness,
it was the spring of hope, it was the winter of despair,
we had everything before us, we had nothing before us,
we were all going direct to Heaven, we were all going direct the other way.

Charles Dickens, "A Tale of Two Cities"

Abstract

Particle Therapy (PT) is an innovative technique that employs high-energy charged ions to treat cancer in an efficient way, taking advantage of their highly localised and controlled energy deposition. Because the distribution of the dose (absorbed energy per unit mass) is peaked at the end of the path, PT is particularly attractive in treating volumes close to organs at risk: side effects like damages to nearby sane tissues are significantly reduced, and the patient can benefit a treatment specifically planned according to his case. One of the most important limitations comes from fragmentation, in particular, during the irradiation, a large fraction of ultra-fast secondary neutrons are produced, that can release energy in nearby tissues, causing an undesired and potentially damaging additional dose both in- and out-of-field. It is crucial to develop a system capable of measuring the contribution to the total energy deposition of these neutrons, their flux and angular distribution, in order to estimate the cross section with respect to human tissues and possibly, through an optimised treatment planning, limit their impact on the efficiency of the treatment. The MONDO project is dedicated to this aim. It has led to the development of a neutron tracker dedicated to the characterization of the ultra-fast secondary neutrons with focus on high detection efficiency, energy resolution and good backtracking capability. The tracker is based on a compact matrix of plastic scintillating fibers coupled with a SPAD array sensor (SBAM), capable to reconstruct the four-momentum of the neutron by measuring the kinematics of recoiled protons produced in double elastic scattering events. An algorithm for event reconstruction, taking into account the full experiment technological and geometrical features, has been developed, to optimise the detector design and study performances of the readout system. The code, working on data from a FLUKA Monte Carlo simulation of the detector studies neutrons in the energy range of [30-450 MeV] and is equipped with a cluster building technique to assembly pixels and reconstruct the proton energy and direction. A method of discrimination between elastic and inelastic events is also employed, and preliminary results on energy and backpointing resolution are presented along with estimates of the reconstruction and detection efficiency.

Acknowledgments

I would like to express my thanks and gratitude to the Applied Radiation Physics Group of Università di Roma “La Sapienza”, for their invaluable help, constant support and shared enthusiasm for this thesis work. Every single member I had the chance to talk to and work with has contributed to all the encouragement, kindness and professionalism this thesis needed. Without taking anything away from the others, I wish to thank the people that backed me up the most during these very “interesting times”: my advisor Riccardo Faccini, his warm welcome and prompt helpfulness immediately made me think I was in the right place; my wonderful co-advisor Michela Marafini, her commitment, experience and guidance have continuously moved and inspired me, and helped me see the silver lining behind every cloud; “l’irreprensibile” Giacomo Traini, I will treasure everything I learned at each problem we had to solve, his patience and mastery are spread all over this thesis; Vincenzo Patera, Alessio Sarti, Riccardo Mirabelli, Giuseppe Battistoni, Eliana Gioscio, Alessandro Bochetti and everybody at the MONDO collaboration, this work owes very much to their passion and skills.

Contents

Introduction	1
1 The Principles of Particle Therapy	3
1.1 Radiation-Matter Interaction	4
1.1.1 Ionization processes	4
1.1.2 Other processes	7
1.2 Useful quantities	9
1.2.1 Absorbed dose	9
1.2.2 Linear Energy Transfer	10
1.2.3 DNA damages: Relative Biological Effectiveness	11
1.3 Treatment planning and particles	12
2 Neutrons	15
2.1 Interaction mechanisms	15
2.1.1 Elastic scattering	17
2.2 Techniques of detection	19
2.2.1 Detection of slow neutrons	20
2.2.2 Spectrum analysis: unfolding	21
2.2.3 Detection of fast neutrons	22
2.3 Secondary neutrons in PT	23
3 MONDO	29
3.1 Detection strategy	29
3.2 Tracker	31
3.2.1 Plastic scintillators	31
3.3 Readout system	33
3.3.1 SBAM: Architecture and DAQ	33
3.4 Monte Carlo simulation with FLUKA	35
3.4.1 SES performances and background evaluation	37
3.4.2 Recoiled protons and DES performances	38
4 Event reconstruction algorithm	41
4.1 Detector geometry and event study	42
4.1.1 Detector geometry	42
4.1.2 Event classification	44
4.1.3 Event display	46
4.2 Clusters and Tracks	48

4.2.1	Clusters building and analysis	48
4.2.2	Track candidates building	50
4.2.3	Direction method and analysis	52
4.2.4	Range and containment study	54
4.2.5	Energy and hardware variables relations	56
4.3	DES events reconstruction	58
4.3.1	Energy	58
4.3.2	Angles	62
4.3.3	Backpointing capability	63
4.3.4	Resolution and efficiency plots	64
	Conclusions	69
	Appendix A	71
	Bibliography	75

Introduction

The first part of the 21st century has seen an astonishing progress in the application of physics to medicine, with innovative techniques of diagnostics and therapies emerging powerfully and giving rise to an exponentially increasing amount of projects and experiments. Particle Therapy (PT), in particular, being one of the most promising and attractive candidates for what is perhaps the greatest challenge in medicine as of today, tumour control, has sparked a lot of discussion and interest. Radiotherapy is still the most popular option for a great number of cancerous pathologies, as therapeutical properties of photons in the X-ray range of wavelengths are well established and have given impressive benefits in the survival rate for treated patients. However, it remains an impracticable option for treating deep solid tumours very close to organs at risk (OAR), since healthy tissues surrounding the tumour inevitably receive an unwanted dose from the photon passage, which can be reduced with methods of focusing and rotation of the beam, but cannot be avoided optimising the treatment planification.

PT differs from conventional radiotherapy for a change of the particles employed as projectiles to irradiate the tumour; instead of photons, PT uses light ions, like protons and carbon nuclei fully deprived of their orbital electrons. The crucial characteristics of these particles is their dose distribution as function of the path inside human tissues; it is a result of fundamental particle physics that charged particles release the greatest amount of their energy within a narrow region of space, located at the end of their path, the position of which depends on the initial energy of the projectile. Therefore, by irradiating the patient with ions at the right energy, it is known where they will interact the most, and the beam can be designed so to damage the tumour with a localised and intense dose, and spare the surrounding healthy body tissue encountered by the particle before coming to rest. In this way, side effects can be greatly reduced, and the patient can benefit from a treatment specifically planned according to his particular case.

One of the most important limitations come from secondary reactions due to the high energy of the particle beam. These give rise to a proliferation of secondary products of nuclear interactions, both charged (protons, electrons, ions etc.) and neutral (photons and neutrons). Determining their impact on the treatment quality and efficacy is considered of vital importance by the medical physics community, and many studies have been carried on this subject. While researches on charged secondaries and prompt photons have led to their progressive integration in the treatment planning system (TPS), ultra-fast secondary neutrons are still an open problem; their production can cause an undesired and potentially damaging additional dose both in- and out-of-field, and are considered responsible for the insurgence

of long term complications such as Secondary Malignant Neoplasms. It is crucial to develop a system to measure the contribution to the total energy deposition of these neutrons, distinguish them from the moderation neutrons background coming from the treatment room (backpointing capability), estimate the frequency of their production and possibly limit their impact on the efficiency of the treatment.

The MONDO project, a collaboration between Museo Storico della Fisica e Centro Studi e Ricerche “Enrico Fermi” (CREF), the Applied Radiation Physics Group (ARPG) of Università di Roma “La Sapienza” and the Istituto Nazionale di Fisica Nucleare (INFN), is dedicated to this aim. It has led to the development of a neutron tracker dedicated to the characterisation of the ultra-fast secondary neutrons with focus on high detection efficiency and good backtracking precision. The tracker is based a compact matrix of plastic scintillating fibers coupled with a SPAD array sensor (SBAM), specifically built for MONDO by ARPG and Fondazione Bruno Kessler (FBK), capable to reconstruct the four-momentum of the neutron by measuring the kinematics of recoiled protons produced by the neutron in elastic scattering events. Several Monte Carlo simulations have given a full picture of the neutron interactions inside the detector and, more recently, on the hardware readout response by the pixel architecture, with optimised geometry and trigger efficiency.

Chapter 1 of this thesis is dedicated to an introduction to Particle Therapy, illustrating its foundation in radiation-matter interactions and the main physical parameters used to determine its efficacy. Chapter 2 will illustrate the problem of neutron detection from both phenomenological and technical point of views, with emphasis on energies of interest for medical physics. Chapter 3 describes the MONDO project for a secondary neutron detector in PT and relevant results of previous FLUKA Monte Carlo simulations that gave estimates on the expected number of interactions and background as well as performances on resolution and efficiency. Chapter 4 will present the first implementation of the event reconstruction algorithm written by the author; its main requirement is to give an estimate on the reconstruction efficiency, backpointing capability and energy resolution using exclusively information from the hardware readout output, and make an event analysis to find the most effective topological criteria for events that give the correct estimate of the neutron four-momentum.

Chapter 1

The Principles of Particle Therapy

Particle Therapy (PT) exploits the properties of energy distribution and dose release of light charged ions to irradiate solid tumours as a valid alternative to surgery, medicines and conventional radiotherapy; for example, if the tumor is close to organs at risk (as in the case of chordomas and chondrosarcomas of the base of the skull), or if the target is especially small, a non-invasive treatment is especially preferable. In order to further distinguish it from radiotherapy with X-rays and electrons (which are also particles), the technique is often called *Hadrontherapy*.

The idea was put forward in 1946 by Robert R. Wilson, at the time leading a project in Harvard for the construction of a cyclotron. Studying the shielding by calculating the interaction with the material of a beam of 100 MeV protons, Wilson found the characteristic dose profile, completely different from the one produced by X-rays, and proposed in a pioneering paper, “Radiological Use of Fast Protons” (published in 1946 in the journal *Radiology*) the use of protons for treatment of solid tumours. It is worth noting that not only Wilson observed the sharp Bragg peak and the almost straight line that protons followed, but he also mentioned the possibility of using helium and carbon ions, writing that “for a given range, the straggling and the angular spread [of heavier nuclei] will be one-half as much as for protons” [29].

Today, 74 years after Wilson’s paper, the vast majority of facilities offering hadrontherapy uses protons and carbon ions¹, at energies of few hundreds of MeV, that have been extensively investigated and are considered the starting point of any further development. Attempts have been made to employ silicon and argon ions, along with neutrons and charged pions, all of which have been progressively abandoned, either for impractical production or poor dose-depth distribution.² Currently, medical physicists are studying other low-Z ions like oxygen, boron and neon as candidates for future usage, varying parameters like Relative Biological Effectiveness (RBE) and Oxygen Enhancement Ratio (OER) [27].

Italy is a pioneering nation, with the first Italian PT center, CATANA (Center

¹Carbon ions are bare nuclei, obtained by removing all six electrons from the atom; what remains is a bound system of 6 protons and 6 neutrons.

²In particular, neutron beams produce a large deposit of energy in the traversed tissues, outside the target volume, causing severe side effects. This is also the reason why medical physicists are concerned about neutral secondary production.

for Hadrontherapy and Advanced Applications), founded in 2002 in Catania, at the INFN “Laboratori Nazionali del Sud”, using proton beams to treat special eye tumors like uveal and conjunctival melanomas. It was followed in 2011 by the CNAO (National Center for Oncological Hadrontherapy) in Pavia; together with the Heidelberger Ionenstrahl-Therapiezentrum, they are the only facilities in Europe offering both proton and carbon ion irradiation. In 2014 the Trento Proton Therapy Center started operation, performing therapies for both paediatric and adult cases.

1.1 Radiation-Matter Interaction

In order to understand the application of particle physics to medicine and plan an efficient treatment, it is necessary to have a solid phenomenological and experimental knowledge of the spectrum of interactions that can happen between matter and radiation, a field with multiple ramifications; the focus of this section will be on processes of energy loss involving charged simple hadrons like protons and carbon ions, since they are the main ingredient of PT.

1.1.1 Ionization processes

When a positively charged particle much heavier than the electron interacts with an atom, the main force at play is the electrostatic one (Coulomb force). The net effect can be a deflection of the particle from its original direction by means of an elastic diffusion, or a loss of energy, caused by an inelastic collision. The energy is transferred to atomic electrons giving rise to ionization processes (the electrons become free from the nuclei) or excitation (transition to external unoccupied orbitals). Given the very large number of processes in order of cm distances, fluctuations in energy loss are negligible for our purposes, and we can define a quantity known as *Stopping Power*, which is the average energy lost by ionization per unit path length. The most used expression of this quantity is the Bethe-Bloch formula.

$$-\frac{dE}{dx} = 2\pi N_A r_e^2 m_e c^2 \rho \frac{Z}{A} \frac{z^2}{\beta^2} \left[\ln \frac{2m_e c^2 \gamma^2 \beta^2 W_{max}}{I^2} - 2\beta^2 - \delta - 2\frac{C}{Z} \right], \quad (1.1)$$

where:

- N_A is Avogadro number;
- r_e and m_e are the classical radius and the mass of the electron;
- β is the velocity of the incoming particle in units of c and $\gamma = 1/\sqrt{1-\beta^2}$;
- z is the incoming particle charge in units of e ;
- ρ , Z and A are the density, the atomic number and the mass number of the target material;
- W_{max} is the maximum energy transferable in a single collision;
- I is the mean ionization potential, the main parameter of the equation, very difficult to calculate theoretically and deduced from actual measurements;

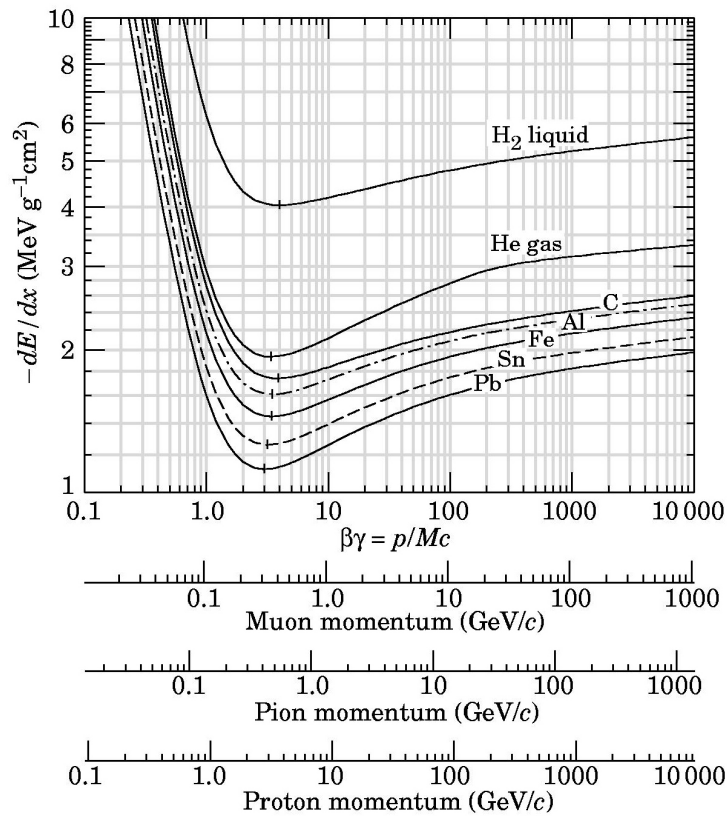


Figure 1.1. dE/dx as function of energy of different incoming particles [26].

- δ and C are two correction terms, called respectively *density* and *shell* correction.

The density effect becomes apparent at high energies and comes from polarization of the target atoms due to the electric field carried by the particle along the path. Since electrons far away from the path are screened by the electric field, their contribution to the total energy loss is decreased. On the contrary, shell correction is important at low energies, particularly when the velocity of the incident particle is of the order of the orbital velocity of the electrons.

The Figure 1.1 shows the Bethe-Bloch formula as a function of the kinetic energy for different types of particles and different ionization materials. In the beginning of the graph, we are in the non-relativistic region; the dominant term is $1/\beta^2$, and different projectiles give distinct curves. At velocities close to $0.96c$, every curve reaches a minimum at an energy approximately independent of the target material; a particle with the corresponding energy is called *minimum ionizing particle*. After the minimum, the function has a slow logarithmic growth, limited by the mentioned density effect.

As the particle is slowed down by successive collisions, it interacts for a longer time, and the energy loss increases. Therefore, the distribution of the absorbed energy per unit mass dE/dm as a function of the distance travelled by the charged particle

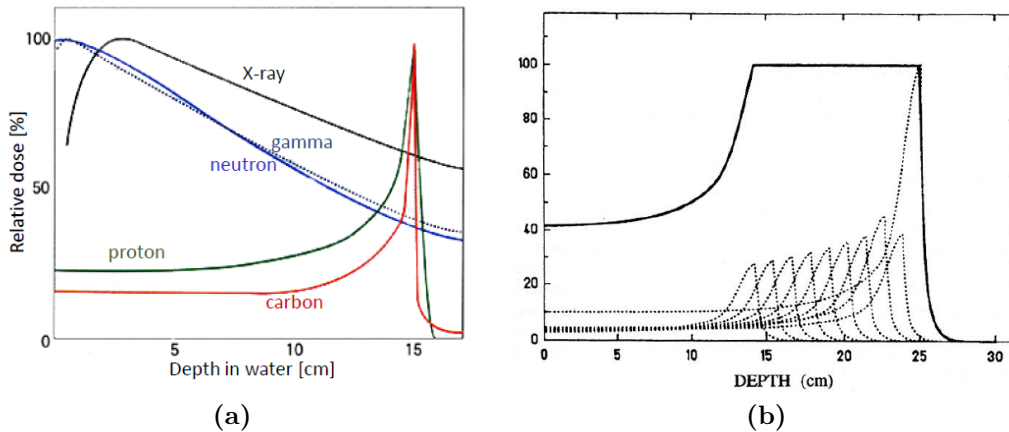


Figure 1.2. (a) Relative dose released on target as function of depth. Protons and carbon ions produce the largest number of ionisations at the end of their path, in a length of few mm corresponding to the Bragg peak. X-rays, on the contrary, release approximately the same amount of energy as they traverse biological tissue. (b) Spread-Out Bragg Peak caused by a beam of protons with different energies able to give a uniform dose to a tumour volume of 10 cm.

shows a characteristic peak at the end of the path. It corresponds to the point where the largest fraction of dose is released, and is named Bragg Peak (BP), after the English physicist who discovered it for alpha particles. The obvious consequence of this characteristic is the chance of concentrating the maximum number of ionisations per millimetre in the tumor area, without affecting the surrounding healthy tissue. The width of the region corresponding to the Bragg peak is usually of a few mm, and the depth depends on the initial beam energy and on the chemical composition of the traversed material. By irradiating the patient simultaneously with particles at different energies, many peaks at different depths are superimposed forming a *Spread-Out Bragg Peak*. This way it is possible to adapt the dimension of the region of maximum energy released on the tissue to cover the whole tumour volume.

The path length is also subject to the phenomenon of *range straggling*, due to the intrinsically stochastic nature of energy loss; the distance a particle with energy E_0 travels before losing all its energy has a Gaussian distribution on first approximation, with an average given by the integral:

$$R(E_0) = \int_0^{E_0} \left(\frac{dE}{dx} \right)^{-1} dE . \quad (1.2)$$

The range is typically measured sending a monoenergetic collimated beam of particles through a target of variable thickness, and measuring the fraction of particles transmitted through. In the Figure 1.3, a typical curve shows the characteristic drop at the end of the path.

To give a simple picture of the advantage of irradiation with protons compared with X-ray beams, the Figure 1.4 shows a comparison between two brain tumour treatments specifically designed to minimize the dose deposited in healthy tissues. It is evident that, even with the best available methods of dose saving, which employs

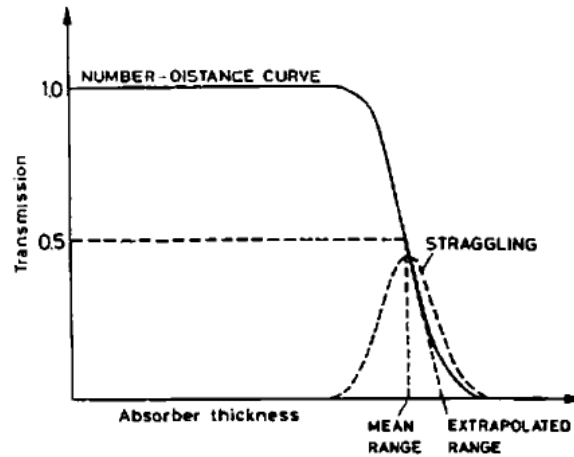


Figure 1.3. An example of a range number-distance curve. As the range is approached, the particles transmitted does not drop immediately to zero; the curve slopes down over a certain thickness with an approximate Gaussian distribution [17].

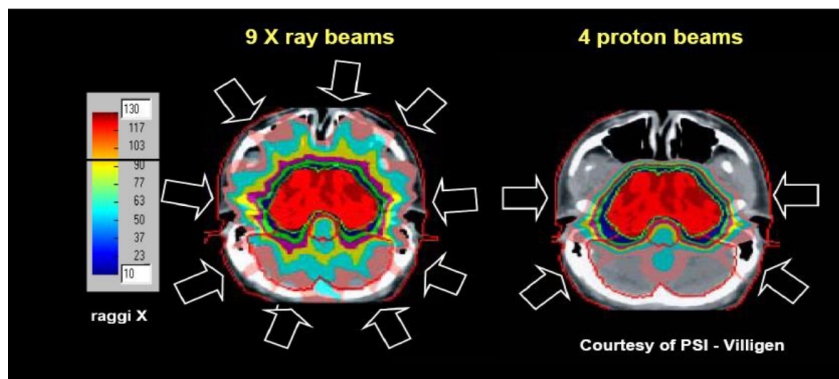


Figure 1.4. Comparison between two treatments done with X-rays (left) and protons (right) done by Paul Scherrer Institut. With fewer beams, proton therapy maximizes the dose on the tumour and minimizes damage on healthy tissues.

techniques of 6-9 non-coplanar beams with non-uniform intensity³, X-rays leave behind them a considerable amount of damaging dose, while protons, delivering the same dose to the tumour area, spare most of the sane tissue, using only four beams instead of nine.

1.1.2 Other processes

The range formula (4.4) does not consider the effect of multiple Coulomb scattering, that deviates the particle from a straight path and has the effect of decreasing the range and spreading the beam laterally. In the limit where we neglect spin effects

³This procedure is called Intensity Modulated Radiation Therapy (IMRT).

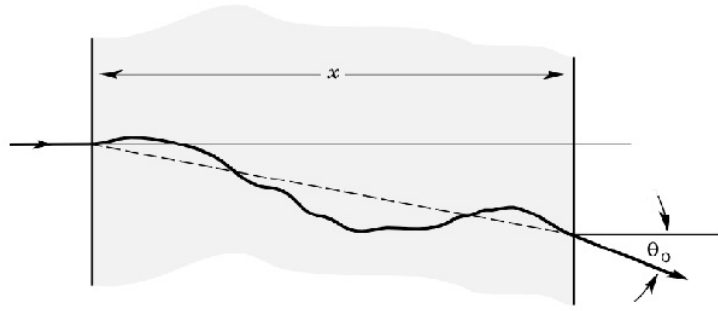


Figure 1.5. Example of path with MCS. The total deflection angle is measured at the end [26].

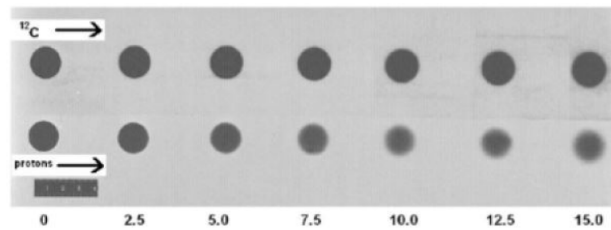


Figure 1.6. Measures of lateral deflection of carbon ion (above) and proton (below) beams. The target is made of water; a film is put at various depths indicated in cm. The difference in the effect of MCS becomes more and more evident at increasing depth.

and screening, the differential cross section is given by the Rutherford formula.

$$\frac{d\sigma}{d\Omega} = z^2 Z^2 r_e^2 \frac{mc/\beta p}{4 \sin^4(\theta/2)} . \quad (1.3)$$

where p and m are the momentum and mass of the incoming particle. The dependence from $1/\sin^4(\theta/2)$ makes the majority of the single angular deflections small. Calculating the net deflection caused by MCS is a problem with many proposed solutions. An empirical formula due to Highland, valid to within 5% for $Z > 20$ and for target thicknesses $10^{-3}X_0 < x < 10X_0$ (X_0 is called *radiation length* of the material) is the following:

$$\sqrt{\langle\theta^2\rangle} = z \frac{20[\text{MeV}/c]}{p\beta} \sqrt{\frac{x}{X_0}} \left(1 + \frac{1}{9} \log_{10} \frac{x}{X_0} \right) \text{rad} . \quad (1.4)$$

The total multiple scattering is due both to the deflection the particles undergo as they are produced in the treatment room (for example with air, exit window, beam pipe, collimators), and while they travel inside the patient. As can be seen from the Figure 1.6, the effect of the lateral spreading is at least 3 times larger for a beam of protons with respect to a beam of carbon ions at the same range. It is thus crucial, especially when using protons, to reduce the material between the exit window and the patient as much as possible.

The other process to consider is nuclear fragmentation, that enters when the particle has sufficient energy (100 MeV or more) to break through the Coulomb

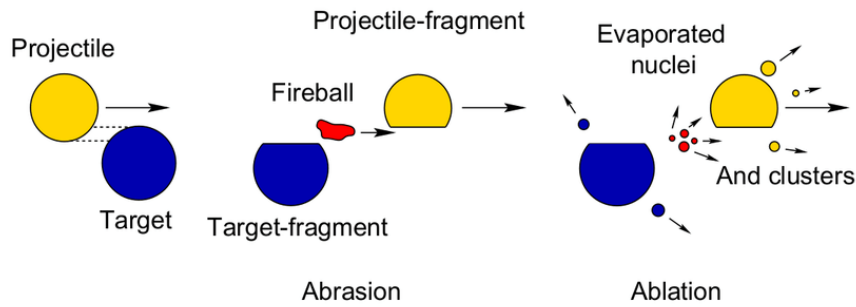


Figure 1.7. Illustration of the abrasion-ablation model of nuclear peripheral collisions at high energies [9].

barrier and interact strongly with the target nucleus. The rigorous analysis of QCD effects is a very complicated subject. To the purpose of this treatment, one can assume that the target is stationary, and the projectile can either impact frontally or peripherally, causing either a *complete* or an *incomplete fusion*. The probabilities of the two reactions are functions of the impact parameter (the lower it is, the higher the chance of a frontal collision), and vary with the energy and the mass of the incoming particle: when the particle goes faster, it is more likely to undergo an incomplete fusion; viceversa, near the Bragg Peak it has a probability around 50% of complete fusion. In the *abrasion-ablation* fragmentation model, the process is divided into two phenomena. In the abrasion step (time of interaction of the order of 10^{-23} s), the overlapping between the projectile and the target creates a secondary residue of nucleons that is separated from the two and is called *fireball*. The remaining piece of the incident particle finds itself in a highly excited state, and as it continues its trajectory (essentially at the same velocity as before) it decays by the emission of photons and/or nucleons; this is the ablation step (characteristic time of 10^{-16} to 10^{-21} s). Target fragments are characterised by high energy release in the zone where they are produced, and short range, while projectile fragments can travel a distance larger than the set beam range, and have the effect of broadening the lateral dose profile.

1.2 Useful quantities

In this section a number of useful quantities will be introduced. Together they define the physics of hadrontherapeutic processes.

1.2.1 Absorbed dose

Perhaps the most important quantity in all processes involving the interaction between radiation and tissues is the *absorbed dose*: it is defined as the average energy deposited per unit mass by means of ionizing radiation.

$$D = \frac{dE}{dm} . \quad (1.5)$$

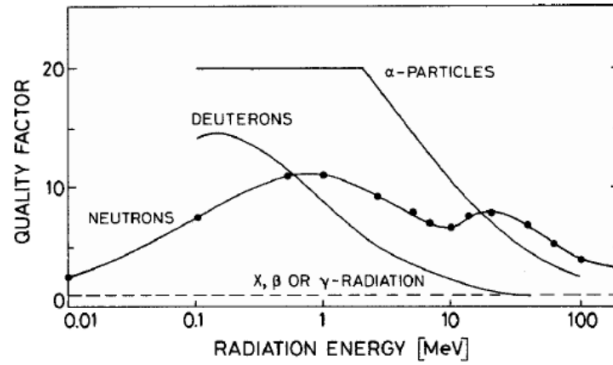


Figure 1.8. Quality factor as function of energy for radiations often encountered in medical and experimental physics [19].

In the International System, it is measured in units of gray (1 Gy = 1 J/kg). Practically, computing the absorbed dose is the first step to determine the biological, physical and chemical effects induced on the target by exposing it to radiation. As such, it must always refer to the material on which the determination is done. The absorbed dose can be linked to the stopping power by means of the equation:

$$D[\text{Gy}] = 1.6 \times 10^{-9} \cdot \frac{dE}{dx} \left[\frac{\text{keV}}{\mu\text{m}} \right] \cdot F[\text{cm}^{-2}] \cdot \frac{1}{\rho} \left[\frac{\text{cm}^3}{\text{g}} \right] .$$

where ρ stands for the density of a thin target and F for the fluence of the particle beam. Defined this way, the absorbed dose is not specific to different particles; this is inconvenient when discussing biological effects, since equal doses of different particles produce effects with intensity varying from one type to another. To account for the specificity, the *equivalent dose* is defined as

$$H = \sum_r D_r w_r , \quad (1.6)$$

where every particle is associated to a particular *quality factor* w_r , which is also a function of the energy. Considering the table, this means that α particles are 2 times more damaging than protons, and these 10 times more than electrons and photons. The equivalent dose is expressed in sievert (Sv); 1 Sv is different from 1 Gy only if w_r is different from 1. The equivalent dose is not a physical quantity; it is a way to express on a common scale the effects generated at low doses by radiations of different quality, so that 1 Sv of α particles has approximately the same effect as 1 Sv of protons, γ -rays, etc.

1.2.2 Linear Energy Transfer

The *Linear Energy Transfer* (LET) is defined as the energy transferred locally⁴ by a charged particle through collisions by unit length. It differs from the stopping power

⁴By “locally” it is usually meant a standard maximum path, or maximum loss of energy, after which the transfer is no more considered local.

because it defines the energy deposited on the region along the primary track, rather than the energy lost by the particle (that has a component due to the production of secondaries like bremsstrahlung photons and high energy electrons interacting far away from their generation point). LET is usually measured in $\text{keV}/\mu\text{m}$, as established in 1962 by the ICRU (International Commission on Radiation Units and Measurements):

$$LET = -\frac{dE_L}{dx} \left[\frac{\text{keV}}{\mu\text{m}} \right] .$$

Referring to it, projectiles can be classified in high-LET (usually higher than $50 \text{ keV}/\mu\text{m}$) and low-LET particles (less than $30 \text{ keV}/\mu\text{m}$). Because of the dynamics of the loss of energy by ionization, a particle can behave as high-LET or low-LET along different parts of its trajectory; particularly, protons release energy at low-LET through the majority of their path, and became high-LET only near the end, at the Bragg peak.

1.2.3 DNA damages: Relative Biological Effectiveness

The tumour is controlled and, hopefully, eliminated by inducing damages to the DNA of the sick cell. The DNA, containing the information for the synthesis of proteins without which a cell cannot live, is located inside the nucleus, a structure with diameter $\sim 6 \mu\text{m}$ (while for the whole cell is $\sim 100 \mu\text{m}$). The damage can be of two types.

- *Direct damage*: it happens when the electrons produced in the ionization directly strike the double helix;
- *Indirect damage*: it is induced by free radicals (OH or H) that forms when the electron interacts with water molecules inside the cell.

In PT, direct damage is always preferable, as it constitutes an injury with less chances of being cured by the cell auto-repairing system. Direct damages are more numerous when the density of ionisation is higher, so they happen mostly at the Bragg peak. The parameter which defines the killing efficiency of ionizing radiation is called *relative biological effectiveness* (RBE). Photons are used as a reference, so that the RBE of a radiation type at a given energy, impacting a certain biological system, is defined as the ratio between the absorbed dose of photons D_{ref} , and the one of radiation of type X that causes the equivalent amount of biological damage.

$$RBE = \frac{D_{\text{ref}}}{D_X} . \quad (1.7)$$

Conceptually, it is equivalent to the quality factor in the equivalent dose, that is in fact a possible expression for RBE. The ratio is calculated by measuring the cellular survival factor with different treatments. The usual parametrization is done with a linear-quadratic model [11]:

$$S(D) = e^{-\alpha D - \beta D^2}$$

where D is the absorbed dose and the two parameters α and β are experimentally determined. Figure 1.9 shows a method of determining the RBE fixing a survival rate value and measuring the intersection with curves for photons and heavy ions radiation.

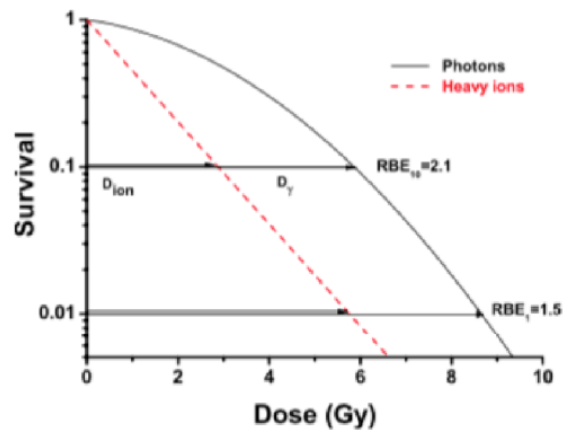


Figure 1.9. RBE values determined for values of cells survival rate of 10% and 1%.

1.3 Treatment planning and particles

PT has many advantages with respect to conventional radiotherapy: it adopts a “conservative” approach in sparing the sane tissues during irradiation of the tumour volume. However, despite its attractive features, it is a double-edged sword; because the net biological effect is maximised on a restricted area, the process needs a constant and efficient monitoring of the treatment parameters. As such, the main issue of hadrontherapy is how to know exactly, at any time, the volume of irradiation and the dose it is receiving. Underdosage of the tumour or an overdosage outside the target volume can happen mostly because of uncertainties in the beam delivery system control and modeling of energy and range; this has to include the internal motion of the patient’s tissue, the uncertainty in the range computation and an additional (organ and position dependent) dose due to both charged and neutral secondary particles being produced in the interaction between the beam of particles and the body. Despite the fact that these unwanted contributions are generally negligible with respect to the main treatment irradiation, over time they can give rise to serious consequences. All of this monitoring activities collectively fall under the name of *Treatment Planning System* (TPS), which usually employs techniques of imaging like PET scans and CT. The software integrated in the TPS can be based on *analytic models* (faster computation, MCS and nuclear reactions not included) or *Monte Carlo methods* (longer time, full description of the interaction). Since they cover a larger set of phenomena, Monte Carlo allow for a more precise definition of the absorbed dose in the tissues, limiting the volume where the beam releases the majority of its energy. However, they require high hardware performances and techniques for reducing the time of computing if they are to be integrated in clinical environment.

Protons at ~ 200 MeV can be obtained either with cyclotrons or with synchrotrons having a diameter of about 7 m. Carbon ions are slightly more difficult to produce; at ~ 400 MeV per nucleon, their magnetic rigidity is 6 Tm, about 3 times larger than protons. For this reason they require about 20 m diameter synchrotrons with magnetic fields in the range 1.5-2 T. Since carbon ions need to be deprived of

six electrons and their higher mass and electric charge require more powerful and weightier experimental setups, a discussion is needed about the advantages of their usage instead of protons. Besides the smaller lateral spreading due to MCS, there are at least two reasons why carbon ion therapy has imposed itself as a powerful alternative. The first is related to precision: at a 200 mm depth, the width of the area with the largest amount of ionisation is approximately 3-4 mm, in contrast with almost 10 mm in proton therapy; the dose distribution with C ions has sharper edges at the border of the treated area, making the dose more localised, which is clinically very important to spare organs at risk. The second, more relevant, is related to efficacy: having an electric charge six times larger than protons, carbon ions slow down more rapidly; to make a comparison, in order to reach a 300 mm depth, they need to have initially about 5000 MeV energy, instead of 200 MeV for a proton. On average, this means that they produce ~ 25 times more ionisations. At the end of the tracks, carbon ions produce many nearby interactions, at typical distance of 2 nm, the transverse dimension of the double helix, or less. If more than one ionisation is caused in such a short segment, what forms is called a cluster of double-strand breaks (DSB), a mostly irrecoverable lesion to the DNA. Moreover, the fact that the most likely damages are direct, the oxygen enhancement ratio (OER)⁵ is reduced and the therapy is more efficient against hypoxic tumours.

The main inconvenient of carbon therapy, and the reason why therapy with nuclei heavier than oxygen are still considered unachievable, is the high production of secondary particles, due to the composite nature of the ion and the high energy at which the beam is set. Typically, the most harmful secondary radiation is due to neutrons in the energy range of 20 MeV to 400 MeV [22]. Suffering no electrical interaction, neutrons can pass through a considerable distance, end up far away from the treated region and release their energy in- and out-of-field, increasing long term risk of developing Secondary Malignant Neoplasm (SMN). The problem is especially relevant in the case of pediatric treatments, where organs have large life expectancies and are very close together [10].

⁵That is the ratio of radiation doses in absence of oxygen (hypoxia) compared to a radiation dose that causes the same biological effect in the presence of oxygen. Its usage in medicine is due to the phenomenon, not yet fully understood, of higher doses needed to treat solid tumours in less oxygenated volumes.

Chapter 2

Neutrons

Neutrons are neutral baryons of mass $m_n = 939.57$ MeV and spin $1/2$. They are stable only when in bound states with protons inside nuclei; as free particles, they β -decay in $n \rightarrow p + e^- + \bar{\nu}$, with mean lifetime $t_{1/2} = 900$ s. The discovery of neutrons dates back to 1932 by James Chadwick at Cavendish Laboratory in Cambridge. Because their energy strongly dictates the most efficient methods of observation, neutrons are classified based on their energy range:

- ultra-cold: $E_n \leq 0.1$ meV;
- cold: $0.1 \text{ meV} \leq E_n \leq 10 \text{ meV}$;
- thermal: $10 \text{ meV} \leq E_n \leq 100 \text{ meV}$;
- hot: $0.1 \text{ eV} \leq E_n \leq 0.5 \text{ eV}$ ¹ ;
- epithermal: $0.5 \text{ eV} \leq E_n \leq 100 \text{ keV}$;
- fast: $100 \text{ keV} \leq E_n \leq 10 \text{ MeV}$;
- ultrafast: $10 \text{ MeV} \leq E_n \leq 100 \text{ MeV}$.

In this chapter the main interactions of neutrons with matter will be discussed, along with techniques of detection and characterization and their production processes in PT, with emphasis on fast and ultra-fast neutrons.

2.1 Interaction mechanisms

Neutrons are uncharged, their main channel of interaction with matter is through strong interactions, and secondarily with products of their weak decay. The range of strong interactions is of the order of 10^{-13} cm (roughly the radius of a nucleon); the absence of long-range Coulombian forces makes the neutron able to cover distances of many cms in matter without interacting, as opposed to particles like protons and electrons. The interaction likelihood and type depend on the target material and on

¹This “cutoff” at 0.5 eV between slow and fast neutrons is about the energy of the abrupt drop in the absorption cross section of neutron beams against a block of cadmium, and as such is called *cadmium cutoff* energy.

the initial neutron energy. Secondary radiation due to interaction of neutrons with matter is almost always made of heavy charged particles; they can be products of neutron-induced nuclear reactions or recoiled nuclei of the absorbing material itself. Thus, neutron detectors frequently use techniques of conversion to extrapolate the characteristics of the primary beam from secondary charged particles that can be directly detected. The main processes that can be identified are:

- elastic scattering: $X (n, n) X$. In this interaction, total kinetic energy and momentum are conserved, and the secondary radiation consists of *recoil nuclei*. It is common to neutrons at all energies, however it is predominantly observed for fast and ultrafast neutrons;
- inelastic scattering: $X (n, n) X^*$. The neutron can lose a greater fraction of its energy than in the elastic case; part of it goes into the excitation of nuclear internal degrees of freedom. The recoil nucleus exits the collision in an excited state, and with the subsequent decay into its fundamental state, emits a γ -ray. Nuclear excitation is a threshold process, so it can happen only if the neutron has a sufficiently high initial energy (usually on the order of 1 MeV or more);
- radiative capture: ${}^A X (n, \gamma) {}^{A+1} X$. The nucleus absorbs the neutron and increases its mass number, becoming an excited state. It quickly decays with the emission of photons². Neutron radiative capture cross-section for low energy neutrons generally decreases as the reciprocal of the velocity as the neutron energy increases (a phenomenon called *1/v law*, valid up to 1 keV);
- other neutron induced reactions, such as (n, α) , (n, p) and $(n, \text{fission})$, where secondary radiations are charged particles, and are thus more desirable than radiative capture for active neutron detectors. They generally occur at energies in the eV to keV interval, and like radiative capture their cross section follows the *1/v law*.

Among neutron reactions important to medical physics are:

- ${}^1\text{H} (n_{\text{th}}, \gamma) {}^2\text{H}$, which releases a 2.22 MeV γ -ray that irradiates the surrounding tissue. It is one of the two important interactions by which thermal neutrons deposit energy in tissue, and is often seen as a background γ -ray in power and research reactors;
- ${}^{23}\text{Na} (n_{\text{th}}, \gamma) {}^{24}\text{Na}$, which activates human blood sodium. The decay of ${}^{24}\text{Na}$ (half life ~ 25 hours, emission of two γ rays) is used to determine the absorbed radiation dose of the patient due to neutron exposure, and serves as monitoring of medical treatment;
- ${}^3\text{He} (n_{\text{th}}, p) {}^3\text{H}$, which is the basis for the use of ${}^3\text{He}$ as a gas in several types of neutron proportional counters;
- ${}^{10}\text{B} (n_{\text{th}}, \alpha) {}^7\text{Li}$, which is used in neutron shielding and as the basis for neutron detectors employing BF_3 gas or boron-lined counter tubes and for Boron Neutron (capture) Therapy.

²Activated photons are instantaneous and can be used to identify the elements present in the sample by studying characteristic lines.

The total probability of interaction for a neutron of fixed energy is expressed in terms of the cross section σ_{tot} per nucleus, as sum of the contribution for each specific process:

$$\sigma_{\text{tot}} = \sigma_{\text{elastic}} + \sigma_{\text{rad. capture}} + \dots$$

If a beam of neutrons is sent across a target material, the number N of detected neutrons per unit volume will fall exponentially with the absorber thickness x :

$$N = N_0 e^{-x/\lambda}, \quad \frac{1}{\lambda} = N\sigma_{\text{tot}}.$$

where λ is the usual definition of *mean free path*. In solid materials, λ is usually smaller than few cms for low energy neutrons, whereas for high energy neutrons it is normally tens of cms.

2.1.1 Elastic scattering

If a collimated beam of fast neutrons is sent across a material, the most likely interactions to occur at first will be elastic and inelastic scattering, that makes the neutron lose energy at every step until it reaches thermal equilibrium with the surrounding atoms. As the velocity reaches thermal values, the cross section for nuclear reactions or radiative capture increases. The slowing down of fast neutrons through energy transfer to matter is called *moderation*, and is a basic process for many applications like nuclear physics and engineering, neutron radiography and tomography.

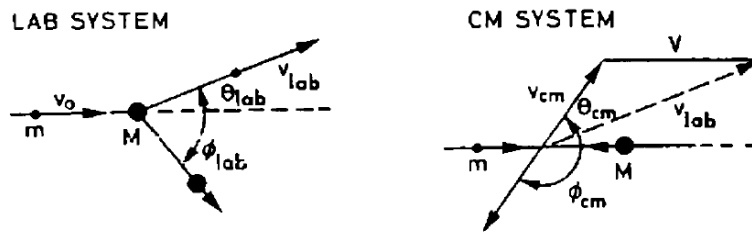


Figure 2.1. Elastic scattering of neutron (m) on a nucleus M in laboratory and center-of-mass reference frames [17].

Elastic scattering is the main process of energy loss in the fast and ultra-fast regions. Neutrons at several MeV of energy can still be treated non-relativistically, for their energy $E \ll m_n c^2$. It is thus possible to consider separately conservations of kinetic energy and momentum in a single elastic scattering of a neutron with velocity v_0 with a nucleus of mass M initially at rest in the lab frame of reference. The neutron mass is customarily put to 1, so that the mass of the nucleus is equal to its atomic mass number A . Going in the center-of-mass (CM) frame, v_0 becomes:

$$v_{\text{cm}} = \frac{A}{A+1} v_0 \quad (2.1)$$

and the nucleus has velocity:

$$V = \frac{1}{A+1} v_0. \quad (2.2)$$

After the collision, the neutron proceeds in a different direction with the same speed as before in the CM system (Figure 2.1). Using Carnot's theorem, the corresponding velocity in the lab system is:

$$v_{\text{lab}}^2 = v_{\text{cm}}^2 + V^2 - 2v_{\text{cm}}V \cos(\pi - \theta_{\text{cm}}), \quad (2.3)$$

where θ_{cm} is the cm scattering angle. Substituting Eqs. (2.1) and (2.2), Eq. (2.3) is rewritten as:

$$v_{\text{lab}}^2 = \left(\frac{A}{A+1}\right)^2 v_0^2 + \left(\frac{1}{A+1}\right)^2 v_0^2 - 2\frac{A}{(A+1)^2} v_0^2 \cos(\pi - \theta_{\text{cm}}). \quad (2.4)$$

Analogously, the ratio between the initial and final energy of the neutron will be:

$$\frac{E}{E_0} = \left(\frac{v_{\text{lab}}}{v_0}\right)^2 = \frac{A^2 + 1 + 2A \cos \theta_{\text{cm}}}{(A+1)^2} \quad (2.5)$$

The scattering angle in the lab frame is instead obtained considering a different cosine relation:

$$v_{\text{cm}}^2 = v_{\text{lab}}^2 + V^2 - 2v_{\text{lab}}V \cos \theta_{\text{lab}} \quad (2.6)$$

which using Eq. (2.4) becomes

$$\cos \theta_{\text{lab}} = \frac{A \cos \theta_{\text{cm}} + 1}{\sqrt{A^2 + 1 + 2A \cos \theta_{\text{cm}}}}. \quad (2.7)$$

The recoil nucleus has energy and scattering angle

$$E_A = E_0 \frac{4A}{(A+1)^2} \cos^2 \phi_{\text{lab}} = E_0 \frac{2A}{(A+1)^2} (1 + \cos \phi_{\text{cm}}) \quad (2.8)$$

$$\cos \phi_{\text{lab}} = \sqrt{\frac{1 + \cos \phi_{\text{cm}}}{2}}. \quad (2.9)$$

From Eq. (2.5), it is evident that the neutron final energy will be comprised in the range

$$\left(\frac{A-1}{A+1}\right)^2 E_0 < E < E_0, \quad (2.10)$$

where the extremes correspond to $\cos \theta_{\text{cm}} = \pm 1$. In the case of collision with hydrogen (a single proton, $A = 1$), the energy lost by the neutron will be:

$$0 < E < E_0.$$

Since the neutron has approximately the same mass as the proton, it can transfer all its kinetic energy in one head-on collision with hydrogen. Thus, it is when the detector material is highly hydrogenous (such as water or paraffin) that moderation and shielding are more efficient.

At energies ≤ 15 MeV, neutron scattering on hydrogen is usually in the *s*-wave channel, which is isotropic. Thus the probability of scattering into a solid angle is

$$dw = \frac{d\Omega}{4\pi} = 2\pi \sin \theta_{\text{cm}} \frac{d\theta_{\text{cm}}}{4\pi} = \frac{1}{2} \sin \theta_{\text{cm}} d\theta_{\text{cm}}. \quad (2.11)$$

From Eq. (2.5)

$$\frac{dE}{E_0} = 2 \frac{A}{(A+1)^2} \sin \theta_{\text{cm}} d\theta_{\text{cm}}, \quad (2.12)$$

so that the energy distribution of a monoenergetic neutron after one scattering is a constant given by

$$\frac{dw_1}{dE} = \frac{(A+1)^2}{4A} \frac{1}{E_0} = \frac{1}{E_0(1-\alpha)}, \quad (2.13)$$

where $\alpha = [(A-1)/(A+1)]^2$. A calculation due to Condon and Breit [6] allows to extract a general formula for the case of n scatterings on hydrogen:

$$\frac{dw_n}{dE} = \frac{1}{E_0(n-1)!} \left(\ln \frac{E_0}{E} \right)^{n-1}. \quad (2.14)$$

Figure 2.2 shows various energy distribution curves at different number of scattering interactions with a generic nucleus of mass A .

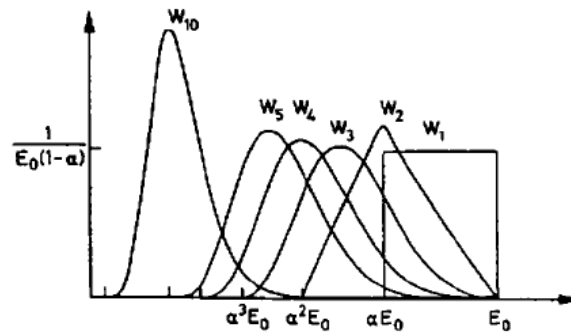


Figure 2.2. With a single scattering, the distribution is uniform between two extremes fixed by kinematics. As the number of interactions increases, the minimum of energy becomes smaller and the curve resembles a Gaussian distribution [17].

2.2 Techniques of detection

Once the mechanism by which neutrons transfer part of their kinetic energy to the target material through collisions with surrounding atoms is established, the discussion can turn towards techniques for detecting the primary beam and studying its properties. The basis principle of neutron detection is the same as the case of charged radiation: converting the neutron variation of energy into a signal, possibly with a certain proportionality to the absorbed energy, that can be interpreted as to retrieve any quantity of interest. The fundamental difference is, of course, that neutrons are uncharged, and cannot produce direct ionisation by interactions with atomic electrons. So, neutron detection requires a *target* to which the particle transfers all or part of its energy to produce secondary charged particles (like p or α) capable to ionize and excite the *detector* material. Since their modes of interaction with matter have probabilities that vary greatly with the kinetic energy of neutrons, the most recommended techniques are different for the cases of fast and slow neutrons.

2.2.1 Detection of slow neutrons

For thermal neutrons, the main reactions to be considered for their detection are absorption with charged secondary production³ : detectors exploit materials with high cross section for nuclear reactions like (n,p) or (n,α) ; in order to maximize the efficiency and keep the size of the apparatus reasonably small, materials with high isotopic abundance are picked, like ${}^6\text{Li}$ and ${}^{10}\text{B}$, or compounds that can be loaded with these elements. Lithium, activated by a neutron, produces a tritium nucleus in its fundamental state. $\text{LiI}(\text{Eu})$ is a particularly good thermal neutron detector: 2 cm of thick cristal have almost 90% efficiency. The reaction on which it is based is the following:

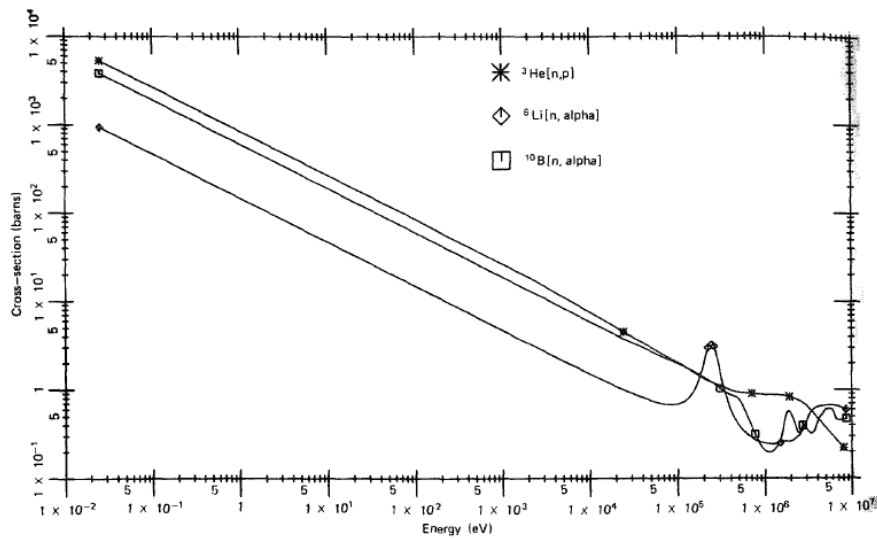
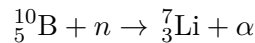


Figure 2.3. Cross section versus neutron energy for reactions most used in slow neutron detection [13].

The detector must also have a high Q -value in order to distinguish as much as possible the secondary products of nuclear reactions from background radiation, like γ and β . For this purpose, glass and liquid scintillators offer the possibility of pulse shape discrimination. Gaseous counters, based on activation of ${}^{10}\text{B}$ nuclei, are often employed for slow neutron detection. The nuclear reaction on which they are based is



where the lithium atom in the final state can be either in the fundamental state or in an excited state with Q -value respectively of 2.792 MeV and 2.310 MeV. Being the latter values much larger than the neutron kinetic energy, these detectors measure the count rate of neutrons, but they are unable to reconstruct their energy. The most used counters of this type contain boron trifluoride BF_3 (elemental boron is

³It is worth remembering that elastic scatterings tend to be very probable even at slow energies, but their effect is mainly to slow down the neutron through moderation, since their energy transfer is so low that detectors have to rely on different processes.

not gaseous). Contrary to scintillators, BF_3 counters differentiate very well neutrons from photon radiation; photons interact with the detector wall creating a background of electrons. The stopping power of electrons is much lower than that of α particles created by neutron interaction, so the electron signal can be easily dealt with.

2.2.2 Spectrum analysis: unfolding

When studying the spectrum of energy of any radiation, the detector will show a *response* function, which gives a measure of proportionality of the radiation energy absorbed by the active medium with the output collected charge, usually converted into an electric pulse (provided that there are no losses and all the particle energy ends on ionisation). The differential pulse height spectrum dN/dH that is recorded from the detector is the convolution of the response function and the energy distribution of the incident radiation. Examples of energy distribution have been shown in Eqs. (2.13) and for neutron elastic scattering. Indicating the incident energy distribution with $S(E)$, so that $S(E)dE$ is the differential number of incident particles with energy within dE about E , dN/dH is given by the integral:

$$\frac{dN}{dH} = \int R(H, E)S(E) dE \quad (2.15)$$

$R(H, E)$ is defined as the differential probability that a particle with energy within dE about E produces a pulse with amplitude within dH about H . Based on the definition, it is easy to verify that, for any value of energy E_0 , $R(H, E_0)$ is indeed the detector response function for a beam of mono-energetic particles. In the case where the energy is fixed, the differential pulse height spectrum will be given by:

$$\left. \frac{dN}{dH} \right|_{E=E_0} = S_0 R(H, E_0)$$

where S_0 is simply the number of recorded pulses. The shape of R usually varies at different energies, and may depend on a number of variables, including geometry, operating conditions, dead time and count rate. If one assumes that all of these are well defined and constant, and the only significant parameter is the radiation energy, when the spectrum is recorded by a Multi-Channel Analyzer (MCA), Eq. (2.15) will be discretised into

$$N_i = \sum_j R_{ij} S_j \quad (2.16)$$

where N_i is the recorded count in the i -th channel, S_j is the radiation intensity in the j -th energy interval, and R_{ij} is the response function coupling each i -th pulse height range with the j -th energy interval.

Assuming that the source distribution is discretised into L such intervals, and the recorded spectrum is made up of M values of N_i , one for each channel, it is possible to write up to M equations of the form of Eq. (2.16), and making a further assumption that the response function is thoroughly known, the system can be solved to determine any S_j provided that $M \geq L$. This method is called *spectrum deconvolution* or *unfolding*. Detection of fast neutrons is one of the main application areas for unfolding techniques [5], as it will be shown shortly.

2.2.3 Detection of fast neutrons

As the energy increases, the cross section for nuclear reactions decreases, and neutrons have less probability to activate nuclei and be absorbed in the material; instead, the apparatus can detect an appreciable amount of energetic recoil particles emitted in elastic scattering, especially protons, since they have a mass almost equal to the neutron and the latter can transfer its whole energy in a single collision (see Eq. (2.10)).⁴ Devices based on fast neutron scattering on protons (hydrogen) go under the name of *proton recoil detectors*. Hydrogen is one of the main components of scintillation materials, so the choice of possible detectors is quite large, from organic crystals (anthracene, stilbene), liquid and plastic scintillators. On principle, nuclear reactions should not play any role, and act as background resonances when using recoil methods.

Since the total kinetic energy is conserved in the reaction, the Q -value of elastic scattering is zero. With a good approximation, the targets are at rest before the scattering, thus it is possible to reconstruct the energy carried in by the incident neutron from the sum of the kinetic energies of the products. At any interaction, the range of energy lost by the neutron can vary from zero to its full energy; if we stay in the approximation that we have used to get to Eq. (2.13), the expected proton recoil energy distribution will be a rectangle, and, on average, the recoil proton will emerge with about half the energy of the original neutron. This simple circumstance is complicated by a number of factors. Unfolding methods can solve the problem of deconvoluting the distortions of the response function from the simple rectangular shape. They are often put in the form of large computer codes, and require a detailed knowledge of the detector characteristics.

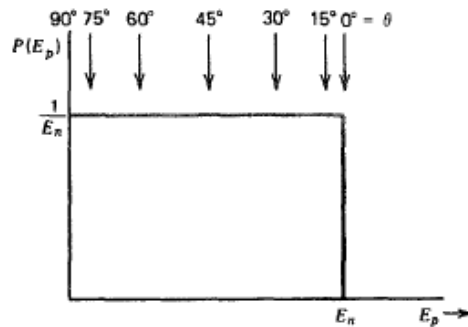


Figure 2.4. Energy distribution of recoil p produced by monoenergetic neutrons. The isotropy of the process is highlighted by the constant value at various recoil emission angles θ [13].

As a first factor to be considered, most organic scintillators does not show a simple linear relation between deposited energy and light output. Instead, the most

⁴Through the process of moderation, the neutron energy is reduced; it is possible to imagine a system combining a *moderating step*, where neutrons are brought to thermal energies, and a slow neutron *detection step*. An example is given by *Bonner's sphere*, proposed in 1960 by Bramblett, Ewing and Bonner [4], whose idea is to wrap a scintillating crystal of LiI(Eu) with spheres of polyethylene with different radii.

common approximation to the distortion caused by *nonlinearity* is

$$H = kE^{3/2},$$

that is, the light output H is proportional to $E^{3/2}$, and the pulse height distribution shape is given by

$$\frac{dN}{dH} = \frac{dN}{dE} \frac{dE}{dH} = k' H^{-1/3},$$

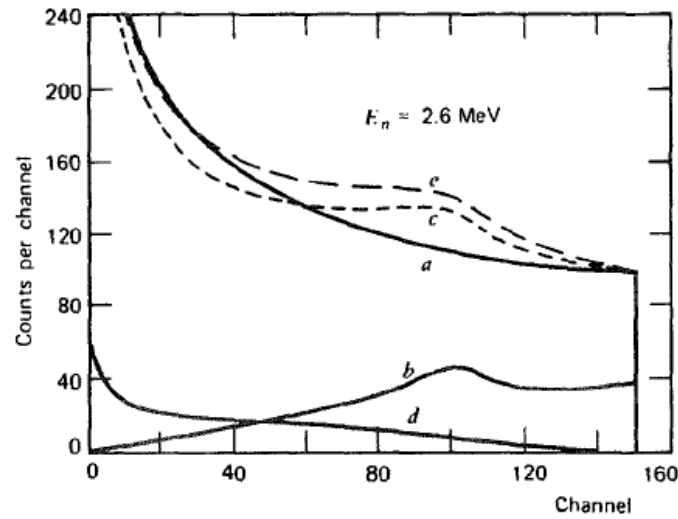
where k and k' are constants. Other effects include: an *edge effect* occurring if the scintillator size is small enough (or neutron energy is high enough) to allow the leak of some recoil protons from the surface of the apparatus, which results on a shift to lower pulse height in the response function; a summation of light from recoil protons produced by *multiple scattering* in a very short time with respect to the pulse shaping time, which adds events at large pulse heights; *scattering from carbon*, present in every organic scintillator, which makes the neutron energy decrease and subsequent scattered proton to emerge from interaction in a smaller range of energy; various sources of noise such as nonuniform light collection, photoelectron statistics and overall imperfect *detector resolution*; *competing reactions* as the neutron energy exceeds 8 or 9 MeV, for which the carbon is also responsible:



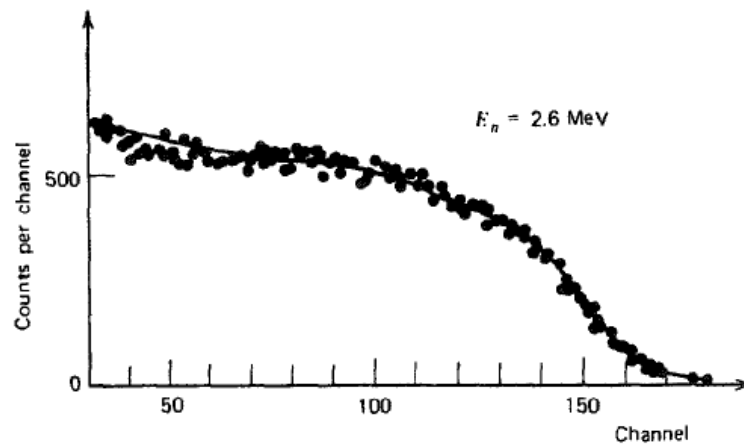
An example of calculation that can be applied to a generally large amount of organic and plastic scintillators for neutron energies below the competing reactions threshold can be seen in Figure 2.5

2.3 Secondary neutrons in PT

Neutrons were among the first particles investigated as valid alternatives to protons in PT, because of their higher penetration depth and greater RBE, which initially gave encouraging results for tumour control rate, especially of radio-resistant tumours. However, their poor depth-dose distribution leads inevitably to a high effective dose released on healthy tissue outside the target volume. For this reason, PT facilities have gradually abandoned neutron irradiation, but a new problem emerges in the form of secondary neutrons production with proton and carbon ions therapies. In the latter case, neutron production is mainly due to nuclear fragmentation, as described in Section 1.1.2. In the first case, the secondary intensity and energy deposit depend on the way the proton beam is produced, collimated and modulated in energy to obtain a reasonable Spread-Out Bragg Peak, and then interaction with organs. This is also the way neutrons are produced in conventional radiotherapy with photons at energy above 8 – 10 MV, by means of photo-nuclear reactions with collimators materials and inside the beam delivery system [25]. Estimates of the dose equivalent per target volume for neutrons following irradiation with protons and carbon ions scanning beam delivery have been performed. The quoted results are, respectively, $5.4 \pm 20\%$ and $2.3 \pm 30\%$ [24].



(a)



(b)

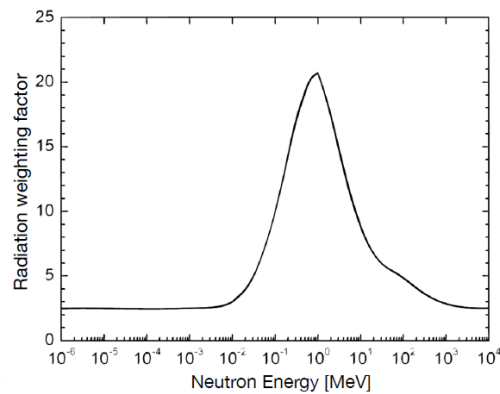
Figure 2.5. (a) An example of calculated response function for a $2.54 \times 2.54 \text{ cm}^2$ cylindrical stilbene crystal with monoenergetic neutrons of 2.6 MeV. Distorting components are continuous lines, resulting responses are dashed. *a*: nonlinearity and edge effects; *b*: double scattering on hydrogen; *c*: combination of single and double scattering; *d*: scattering on carbon; *e*: sum of *c* and *d*. (b) Experimental pulse height spectrum for the same crystal, adding to the previous computation the evident imperfect detector resolution [13].

Studies are undergoing to detail the relation between the presence of secondary neutrons in therapy and the occurrence of Secondary Malignant Neoplasm (SMN), since they are unavoidably present also in conventional radiotherapy treatments, and the survival rate of children with cancer is growing year by year: the incidence of SMNs 30 years after the end of treatment is around 10 – 20 %. The weighting factor w_r due to neutron radiation from the definition of equivalent dose (Eq. (1.6)) has been computed varying the incident neutron energy; the dependency is strong, and is described by the equation [12]:

$$w_r = \begin{cases} 2.5 + 18.2 \cdot \exp\left(-\frac{(\ln E_n)^2}{6}\right) & E_n < 1\text{MeV} \\ 5.0 + 17.0 \cdot \exp\left(-\frac{[\ln(2E_n)]^2}{6}\right) & 1\text{MeV} \leq E_n \leq 50\text{MeV} \\ 2.5 + 3.25 \cdot \exp\left(-\frac{[\ln(0.04E_n)]^2}{6}\right) & E_n > 50\text{MeV} \end{cases} \quad (2.17)$$

Incident neutron energy (E_n) in MeV	Radiation weighting factor (w_R)	Incident neutron energy (E_n) in MeV	Radiation weighting factor (w_R)
1×10^{-6}	2.5	0.4	18.3
1×10^{-5}	2.5	0.5	19.3
1×10^{-4}	2.5	1.0	20.7
1×10^{-3}	2.5	2.0	17.3
5×10^{-3}	2.7	4.0	13.3
1×10^{-2}	3.0	6.0	11.1
5×10^{-2}	6.6	8.0	9.7
0.1	10.0	10.0	8.8
0.2	14.3	20.0	6.8
0.3	16.8	40.0	5.7

(a)



(b)

Figure 2.6. (a) Values of neutron radiation weighting factor as recommended by the latest International Commission of Radiological Protection [12]. (b) Weighting factor as a continuous function of the incident neutron energy [22].

The consequence is that neutrons are more dangerous in the middle energy range, where the weighting factor can be up to 20. The weighting factor is then used concurrently with the distribution of secondary neutrons produced in human tissue as function of the energy to get their net effect on the treatment. The production distribution in Radiotherapy and PT strongly depends on a wide number of variables, including specifics of the treatment (organ placement, energy and intensity of the beam), the patient (age, sex, physical characteristics) and even treatment units using different experimental techniques and different dosimetric protocols [2]. Figure 2.7 shows the measured neutron spectra induced by a 25 MV photon beam [16] and by a 200 MeV/u carbon ion beam [10]. As can be seen, the largest fraction of secondary neutrons produced in carbon ion treatment is in the fast and ultra-fast region (energies up to 220 MeV).

A convolution of the neutron emission spectrum and the trend of the weight factor as function of the energy is shown in Figure 2.8. It needs to be emphasised that, even though it would seem, by looking at their weighting factor, that neutrons are emitted in an energy range that is not very dangerous compared with the spectrum

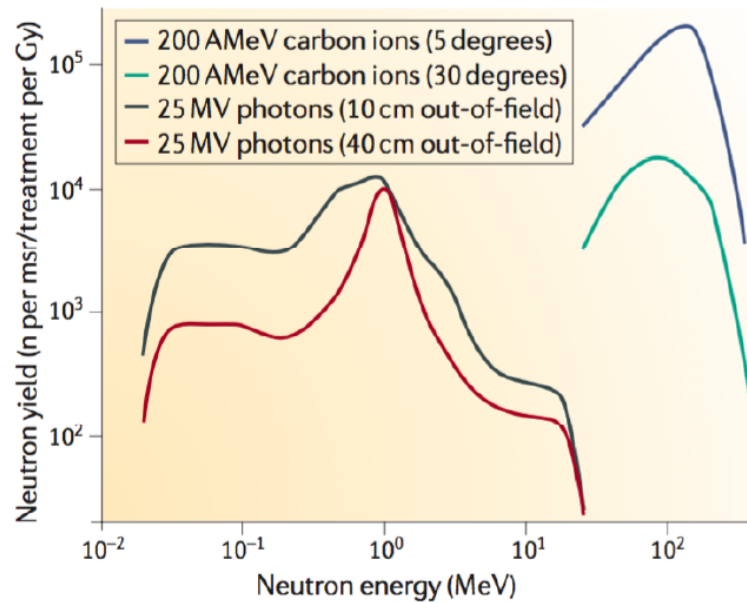


Figure 2.7. Emission spectra of secondary neutrons produced during treatments with 25 MV photons at Linac ELEKTA, Klinikum Goethe Universitat, and carbon ions $E=200$ MeV/ u at GSI, Darmsadt [22].

generated by photons, by the process of moderation they begin to lose energy via multiple scatterings, and can reach $E_n \simeq 1$ MeV before exiting the patient, entering the more damaging region. Another point to make is that measurements from non-directional detectors are affected by the background of neutrons coming from the treatment room, scattered by air, materials and personnel. Detection techniques currently available for neutrons does not allow for a complete characterization of their direction and energy, and this increases the overall measurement systematic uncertainty.

The MONDO project, which will be the subject of the next chapter, is dedicated to building a tracker for secondary fast and ultra-fast neutrons emitted specifically inside the patient, during a PT session, measuring its energy and direction, and providing with a comprehensive overview of their effect on the treatment planning.

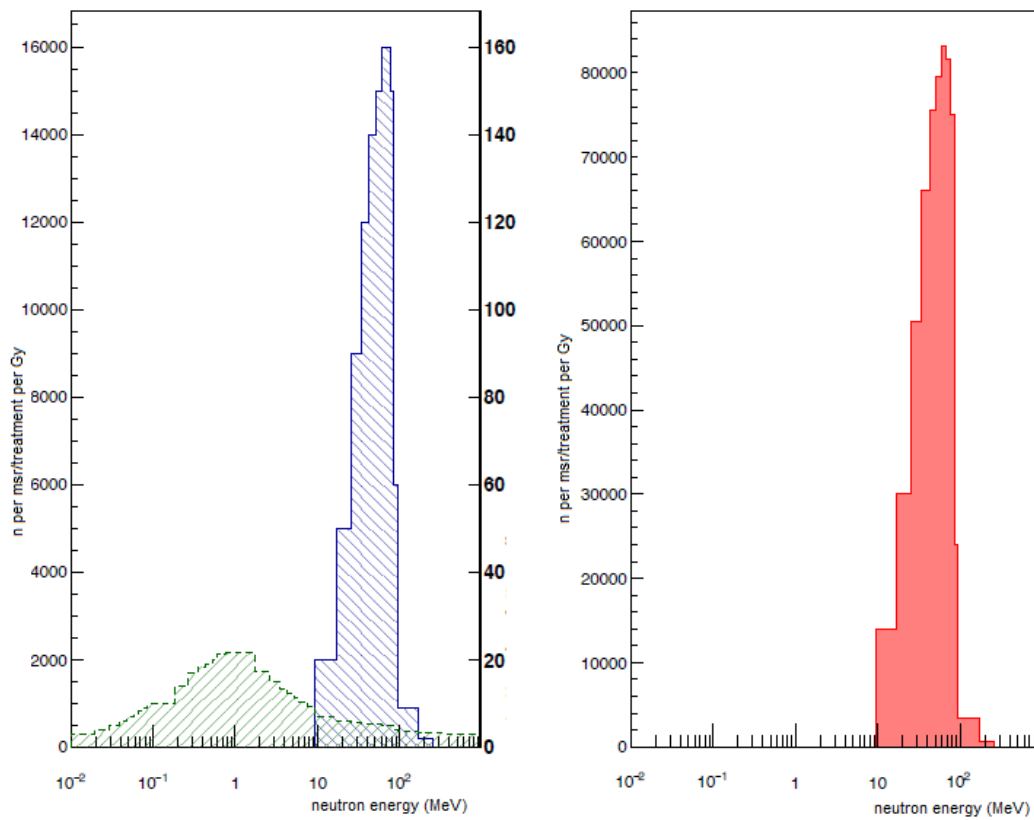


Figure 2.8. Convolution of secondary neutrons emission (continuum) and weighting radiation factor (dashed) spectra as function of energy.

Chapter 3

MONDO

For reasons we have illustrated in the first chapter, the need for a systematic characterisation of the secondary neutron spectra in PT has emerged. MONDO (MOnitor for Neutron Dose in hadrOntherapy) is specifically designed to:

- provide a precise measurement of the neutron flux, energy spectrum and angular distribution, allowing to predict the normal tissue toxicity and the risk of complications;
- work integrated in the clinical environment, being able to discriminate secondary neutrons from the ternary neutral component coming from iterative interactions of fragments with the treatment room and the patient, exploiting the high efficiency and background rejection capability of the detector;
- improve the experimental precision on measurements of the cross section for the process of double differential production of neutrons in carbon irradiation of tissue equivalent compounds.¹

This chapter will illustrate the MONDO detector and readout system, from its phenomenological grounding in neutron elastic scattering to the building of its structure prototypes, together with results of the most recent simulation characterisation and measurements.

3.1 Detection strategy

The MONDO tracker aims at reconstructing the properties of the secondary ultra-fast neutrons produced in PT by looking at a particular process that allows to extract the most useful amount of information: double elastic scattering reactions (DES) [18]. As described in Chapter 2, in a single elastic scattering, the interaction changes the incoming neutron momentum and generates a recoil proton whose kinetic energy depends, by conservation of the four-momentum, on that of the primary neutron by

¹Incidentally, this is very interesting from the perspective of possible applications for other urgent problems like monitoring the radiation field outside the shielding of high-energy accelerators, and radio-protection for astronauts for long-term space missions [14].

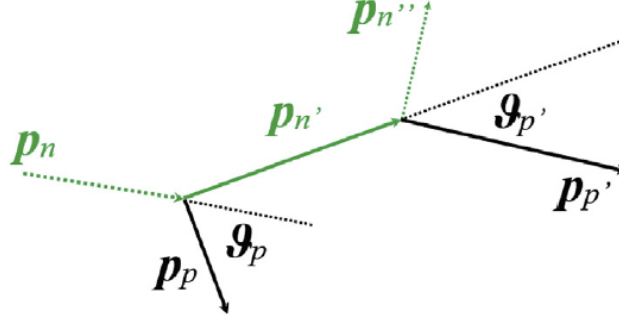


Figure 3.1. Representation of the double elastic scattering interaction. The neutron path is shown as a green line, recoil protons as black.

the equation:

$$\begin{aligned} \vec{p}_n &= \vec{p}_p \frac{1 + m_n/m_p}{2 \cos \theta_p} \simeq \frac{\vec{p}_p}{\cos \theta_p} && \text{because } m_n \simeq m_p \\ E_n &= \frac{2E_p m_p}{\cos^2 \theta (E_p + 2m_p + E_p/\cos^2 \theta)} \simeq \frac{E_p}{\cos^2 \theta} && \text{if } E_n \ll m_n \end{aligned} \quad (3.1)$$

where (E_n, \vec{p}_n) is the initial neutron four-momentum, (E_p, \vec{p}_p) is the recoil proton four-momentum and θ_p is the angle between directions of the two particles (see Figure 3.1 for reference).

The neutron four-momentum can be reconstructed by applying Eq. (3.1) to both first and second interactions. First reconstruct p_p and p'_p by range measurement; then measure the distance between first and second interaction vertexes and the angle it spans with the second proton track to get θ'_p ; p'_n is then uniquely determined by Eq. (3.1), and p_n by conservation of momentum; finally, θ_p is determined applying once again Eq. (3.1)². Concretely, the MONDO detector is designed to simultaneously determine the direction and the range inside the target material (extracting the kinetic energy) of both recoil protons produced in a DES reaction, at the same time rejecting the background contribution due to moderation processes in the environment; with these information, it is possible to retrieve the emission profile of the neutron.

Plastic materials are highly hydrogenated, increasing the probability of the neutron to interact with single protons and obtain elastic scattering events (Eq. (2.10)). If the two recoiled protons released consecutively remain inside the detector, the proton range can be determined with the number of traversed fibers. The energy released by the recoil proton as scintillation light is collected by the readout system, which will be discussed in detail. Additionally, plastic materials contain carbon, also subject to neutron elastic scatterings, with much smaller recoil energy useless to the aim of reconstruction. It is clear that, because neutron characterization requires two independent measurements on recoil protons, the tracker achievable energy and spatial resolutions will be the main features for its successful application.

²The same amount of information cannot be extracted with a single elastic scattering, in which case it is not possible to know both energy and direction of the incoming neutron just from the reconstructed proton energy.

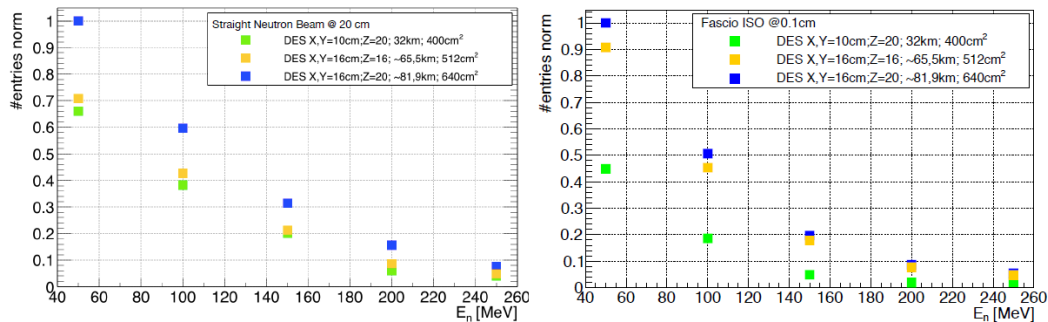


Figure 3.2. Monte-Carlo evaluation of reconstructed DES events as function of the primary neutron beam energy for three detector sizes (data normalised to the highest counting rate). The left figure refers to a setup with a neutron source shooting straight particles from a distance of 20 cm from MONDO. The right figure is obtained with an isotropic source at 1 mm distance. Additional information reported are the length of fibers needed in km and the total area covered by all the layers.

3.2 Tracker

The targets, that serve also as the active component of the detector, are 800 layers of thin squared plastic scintillating fibers with thickness $250 \mu\text{m}$, arranged in orthogonal x-y planes, to allow for three-dimensional reconstruction of the incoming particle. The thickness value has been chosen to maximise the granularity on the proton track, thus enhancing the achievable spatial resolution and lowering the threshold on low energy protons up to roughly 12 MeV [7], that on average travel distances $\sim 1 \text{ mm}$, and are thus able to cross at least 2-3 in both x-y planes, the necessary condition to deduce the neutron energy and direction. The detector volume has been chosen by computing the average length of interaction inside plastic fibers of neutrons in the energy range 20 – 400 MeV, whose maximum value is about 10 cm, and taking a compromise between high detection efficiency and reasonably low cost of production. The chosen active volume of the fibers matrix is $16 \text{ cm}^3 \times 16 \text{ cm}^3 \times 20 \text{ cm}^3$ [20].

3.2.1 Plastic scintillators

Plastic fibers for MONDO have an active volume largely made of polystyrene (PS), which from the chemical point of view is a long chain of carbon centers and benzene rings (C_6H_6). The interaction takes place inside the *core* area, which is coated inside one or more layers of *cladding* of a few μm of thickness. A fraction of scintillation light is produced following the passage of a charged particle in the core; light rays crossing the interface region between core and cladding at angles of incidence larger than the critical angle for total *internal reflection* are conducted to the readout end. The critical angle is given by the well-known relation:

$$\theta_c = \sin^{-1} \frac{n_1}{n_0},$$

where n_0 and n_1 are the refractive indices of the areas from where the light comes and to where it moves respectively. MONDO uses squared scintillating fibers with *single cladding* of PMMA (polymethylmethacrylate) about $200 \mu\text{m}$ thick, together

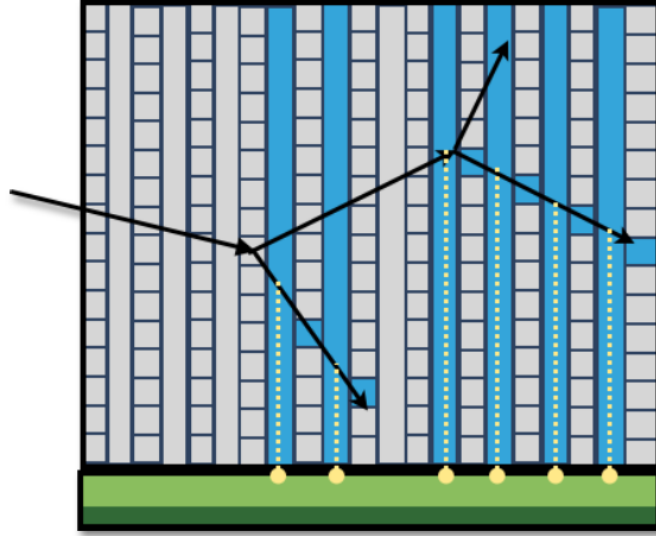
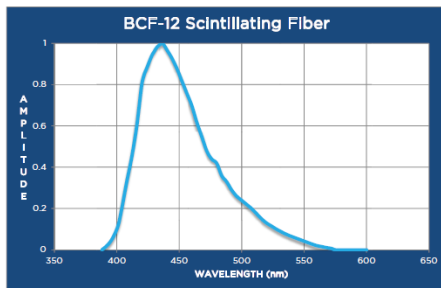


Figure 3.3. Geometry of the MONDO tracker. Fibers activated by passage of a charged particle are highlighted in blue, and the signal propagates along the yellow lines.



Material	Polystyrene
Cladding thickness	4% of diameter
Trapping efficiency	7.4%
Decay time	3.2 ns
Light yield	8000 photons/MeV
Emission peak	435 nm
Attenuation length	2.7 m

Figure 3.4. Light yield for Saint-Gobain scintillating optical fibers (BC-12), with table summarizing main properties [23].

with another type of fibers covered with an additional external layer of a derived fluor-acrylic compound (*double-cladding*), that allow for a higher trapping efficiency and lower transmission of photons between nearby fibers (cross-talk). Polystyrene has a refraction index $n=1.60$, while the cladding has $n=1.49$ for the first layer and $n=1.42$ for the second one, when present.

MONDO plastic scintillating fibers are manufactured by Saint-Gobain [23] (double cladding) and Kuraray (single cladding). Their emission spectrum, to be carefully taken into account when studying the most appropriate and efficient readout method, is shown in Figure 3.4 and Figure 3.5.

Tests on calibration and efficiency of the tracker were performed at the APSS Proton Center on a prototype called *Penelope*, consisting of a $4 \times 4 \times 4.8 \text{ cm}^3$ block of double cladding scintillating fibers. While the first readout was performed through a standard PMT multi-anode, the second readout used an innovative

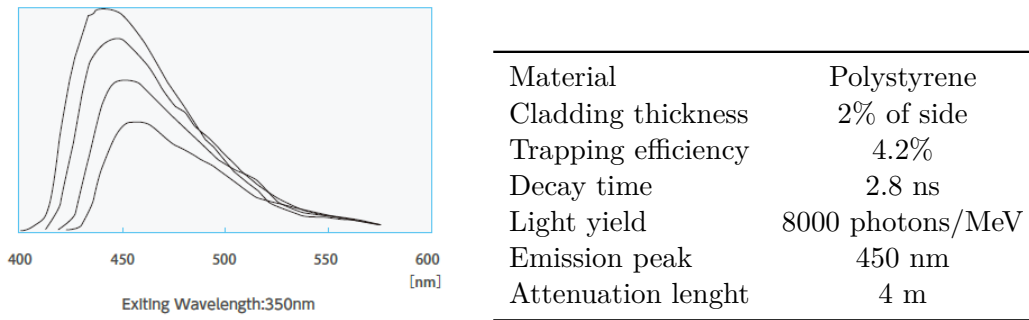


Figure 3.5. Light yield for Kuraray scintillating fibers (SCSF-78), with table summarizing main properties. The 4 spectra correspond to different fiber lengths, respectively (starting from the top) 10, 30, 100, 300 cm [15].

silicon-based single-photon avalanche diode (SPAD) array sensor, developed in collaboration with Fondazione Bruno Kessler (FBK)³ specifically for MONDO. Good results on comparison between experiments and simulation [7] encouraged further implementation of SPAD technology in the MONDO project, and led to the realisation of the final readout system.

3.3 Readout system

The MONDO detector needs a dedicated digital readout system with single photon sensitivity that can work with the high number of channels, granularity and compactness of the active medium. SPADs are solid state semiconducting devices with CMOS (Complementary metal-oxide-semiconductor) operating principle. Inside, there is a p-n junction with high doping density. The photon is detected by the production of an electron-hole couple; they are directed, by means of a strong electric field, towards two electrodes, gaining momentum and ionizing atoms in the lattice along their path with an avalanche effect; the result is an augmented charge production and a sizable electric signal. The acquisition system collects the signal and stores the information in digital form. When this is done, the avalanche is stopped by turning down the electric field with a circuit of *active quenching*. As the avalanche is still ongoing, an additional signal induced by a new photon cannot be read, bringing a finite dead time to the acquisition.

3.3.1 SBAM: Architecture and DAQ

The final readout sensor, called *SPAD Based Acquisition for the MONDO experiment* (SBAM) consists in arrays of elementary detection cells, the circularly shaped SPADs with active diameter of $\simeq 16 \mu\text{m}$, coupled with electronics and circuitry; this structure is called *pixel*. SBAM has pixel size tuned on the fiber thickness ($125 \times 250 \mu\text{m}^2$), time resolution per pixel of $\sim 100 \text{ ps}$, and an implemented double threshold self-triggering logic that can sense signals up to few photoelectrons with a dark count

³<https://iris.fbk.eu>.

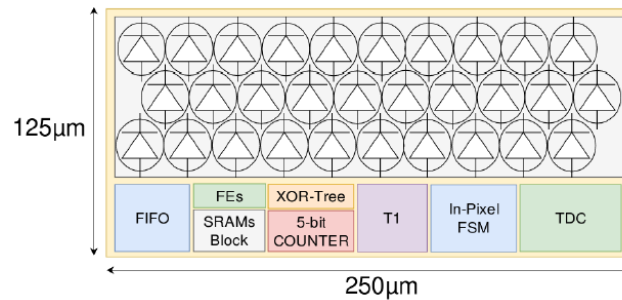


Figure 3.6. Pixel schematic design [20].

rate (DCR) of about 1 kHz [21]. Chips consisting of up to 3200 pixels have been assembled, with total area close to 1 cm². Each pixel includes:

- 3×10 SPADs arranged as in Figure 3.6 (Fill Factor, e.g. the relative pixel active area $\sim 30\%$);
- circuit of Front-end electronics (FEs) with the aim of compressing the SPAD pulses from their typical spread of 100-200 ns to an interval comparable with the expected timing of the signals, about 5-10 ns;
- an integrated SRAM block allowing to individually enable/disable each SPADs, very useful when dealing with noise produced by high DCR;
- XOR-Tree circuitry that compresses further the SPAD pulse to few hundreds of ps and fuses signals from different SPADs in a single line, feeding its output to a 5-bit fast photon counter as input triggering clock;
- a 10-bit Time-to-Digital Converter (TDC), controlled by a Finite-State machine (FSM) specific to the pixel, with the responsibility of monitoring the TDC activity and setting supplementary data flags.

The most relevant features of SBAM are mentioned in Table 3.1. The data acquisition is managed by a Xilinx SP605 board with an FPGA Spartan-6 inside. The sensor manufacturers provided also a computer interface for user control and setting of the acquisition. The possible operations are: switching on and off singularly SPADs for DCR control; choose between self-trigger mode or external triggering with a user-generated signal; set the threshold for the photon number prompting acquisition; fixing the time window for acquisition, that is the number of *clock times*, each of which is 10 ns long. The output data are space, current and time parameters of the event, for example how many photoelectrons have been detected, the position of the flashed SPADs inside the pixel, and the instant at which the acquisition took place in ps.

The MONDO setup considered up to now will be covered laterally by chip tiles of about 4×4 cm². Figure 3.7 shows a yet to be finalised positioning of the chip on the tile area around the detector. The limiting factors to be taken into account are the dead space between two adjacent chip, the positioning of the input/output pins needed to configure the sensor and the connection with the DAQ system. Figure 3.7

Table 3.1. Summary of SBAM performances [20].

Parameter	Sensor characteristics
Pixel Size	$250 \times 125 \mu\text{m}^2$
SPADs/Pixel	30
Pixel fill factor	32.1%
SPAD median DCR	500 Hz
TDC resolution	80 ps
Trigger	Double threshold
Power consumption	57.7 - 57.4 mW
Frame rate	20 kHz

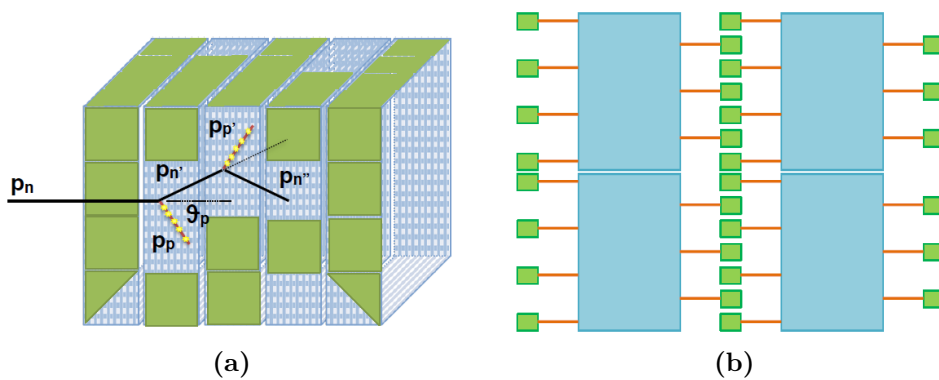


Figure 3.7. (a) MONDO fibers matrix with schematic representation of the chip tiles based on SPAD arrays. A DES event is superimposed. (b) Example of a possible SBAM chips disposition. Chips are displayed as blue rectangles, bonding wires as red lines and input/output pins as green boxes.

displays also a possible implementation of SBAM sensor chips on a tile. The dead space is reduced putting asymmetric bonding on the two sides of the chip, so that pins dedicated to input and output of two adjacent chips share the same space area, standing on a single line.

3.4 Monte Carlo simulation with FLUKA

Since the beginning of the digital revolution, it has become customary for experimental physicists to use software tools that can simulate in great detail several millions of events of a given process, knowing the cross section of all the interactions at play. With this procedure, it is possible to obtain a large amount of information and a comprehensive picture of all the possible variants of the event weighed with the appropriate occurrence probability and cleansed from external factors like spatial boundaries, time limits, dissipation of energy and deterioration of materials⁴. The method of simulation is called Monte Carlo, and it is based on successive random

⁴Of course, all this effects can also be simulated, given an appropriate model of parametrization, to predict the real working conditions of the experiment.

generation of numbers. Most Monte Carlo-based codes work in the following steps:

- the impending radiation characteristics are defined, that include the type of particle, its energy and the probability of interactions of interest; the target is also defined, particularly its geometry, composition of materials, optical properties and position with respect to the incoming particle direction;
- an elementary sampling volume, the value of which is determined by the user, is given to the method to decide the frequency at which the computation of the interaction probability needs to be restarted and the results stored;
- as the virtual particle enters the target zone, the method follows its path and, at each discrete step, generates a set of random numbers according to the probability distribution of the phenomenon one wishes to investigate. The numbers determine whether the particle undergoes an interaction or proceeds undisturbed;
- the particle, and the set of eventual secondaries produced, enters the next step of sampling and another set of numbers is generated, without any memory of the previous computation;
- the process stops if all the particles are brought at rest or exit the interacting volume.

It is also possible to introduce threshold functions to exclude interactions not relevant at considered energies, in order to reduce the time of computation. Through the modelling of the tracker readout system, the information about the interaction is transferred to a virtual signal produced by the simulated apparatus.

FLUKA [1] is a simulation package for particle physics equipped with many interaction and transport phenomena, developed by researchers at INFN (Istituto Nazionale di Fisica Nucleare) and CERN (Conseil Européen pour la Recherche Nucléaire); due to its high versatility, it is used in various experimental physics environments, such as dosimetry, cosmic rays analysis, accelerators shielding, radiotherapy and PT⁵. The simulated particles can be of about 60 different types, with energies up to 20 TeV, and the geometry can be rather complex and with different materials and densities inside, allowed by the CG (Combinational Geometry) package. For every particle inside, FLUKA computes the interaction probability and produces a simulated process, scoring nature, position and time of interaction and kinematical parameters of exiting particles. The storage of the useful amount of information is conducted using ROOT, a much used data and graphic framework in high energy physics written in C++ language, developed by CERN.

The data present in the ROOT output file are processed in two complementary ways. On one hand, the MC truth is used for direct analysis of the process. At this level, it is interesting, for example, to compute the probability of observing a particular process, or a given population of particles of a certain type and energy, observe how many particles remain inside the detector, study the tracker response at pixel level and correlation of parameters. The values to be used are directly

⁵FLUKA is the main IT tool with which physicists are studying the possibility of employing different ions in PT, such as helium and oxygen.

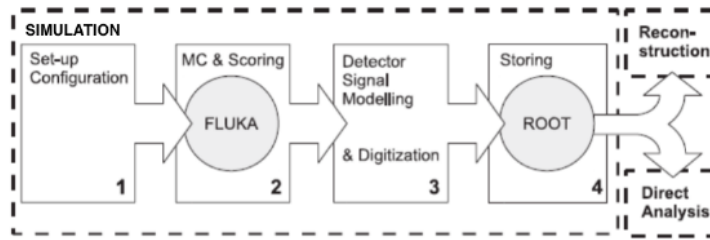


Figure 3.8. Steps of MC simulation and analysis.

obtainable by the simulation, without any additional handling. The second kind of analysis goes under the name of reconstruction; the data about the pixels (position and collected charge) are treated as in the context of an experimental environment, and a parametrization is applied to them to reconstruct the event at the particle level. For this thesis work, this meant grouping nearby pixels into clusters, supposed to be manifestations of the passage of a single particle inside the material, and by an energy-range relation and topology considerations, identify the configuration with the best chance to describe a double elastic scattering event. The strength of the reconstruction algorithm is put to the test of efficiency and resolution calculation.

3.4.1 SES performances and background evaluation

In 2018-2019, MONDO expected performances have been evaluated using the FLUKA code with a modelled tracker of $800 \times 250 \mu\text{m}^2$ fibers arranged in x - y planes, for a total detector volume of $10 \times 10 \times 20 \text{ cm}^3$. The results [7] on energy resolution using single elastic scattering on protons and anelastic background evaluation are presented in Figure 3.9. The neutrons enter the detector with an energy in the range between 50 and 300 MeV, and their momentum is reconstructed with Eq. (3.1)⁶. The proton kinetic energy is extrapolated from the range by using the energy-range relation proposed by Bortfeld and Schlegel [3] and fitting the proton energy in the interval 10-250 MeV with the values of the range according to NIST. The angle is computed with a linear fit on the proton track. The energy resolution for neutrons interacting with a single elastic scattering is between 4% and 11%. The percentage error on the angles increases with energy, because neutrons at higher energies tend to produce secondaries at smaller angles. On the contrary, the energy resolution decreases for shorter proton tracks, produced at low energies.

The other plot shown in Figure 3.9 shows the number of elastic and inelastic collisions per primary neutron in the MONDO detector, as a function of the neutron energy of monochromatic neutrons between 20 and 300 MeV. Inelastic interactions covering up (or misinterpreted as) double elastic scatterings represent the main background of the neutron characterization. Only protons crossing at least 3 fibers in both planes are considered. As can be seen, the single elastic interaction is dominating below 70 MeV; at energies higher than 100-150 MeV, inelastic events

⁶As it has been discussed, this procedure is impracticable in MONDO without knowing the primary neutron direction. However it is useful to consider to study the model capability of reconstructing a single proton energy and direction. Moreover, there are other cases in which the direction is known, as in neutron beams monitor applications or measures of cross sections.

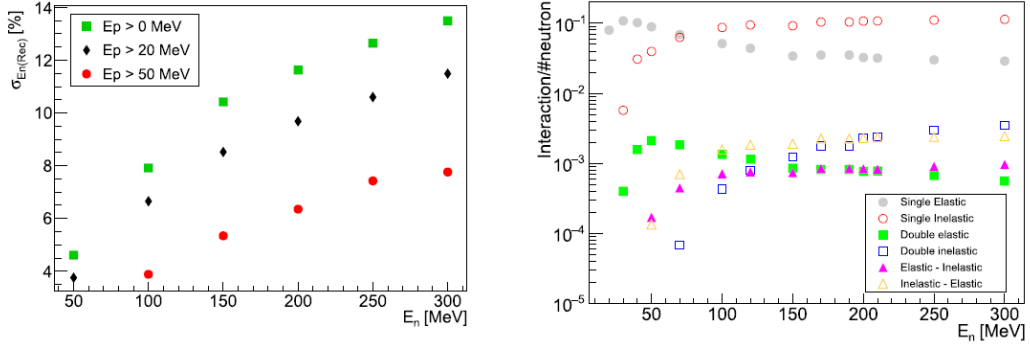


Figure 3.9. (Left) Neutron energy resolution as function of the initial kinetic energy. The direction is supposed to be known so that a single elastic scattering with a proton is sufficient to reconstruct the neutron momentum. More energetic protons have longer tracks and allow for a better achievable precision. (Right) Number of interactions per primary neutron as function of its kinetic energy. Elastic events dominate at energies below 100 MeV, whilst inelastic interactions become more numerous at higher energies. The rate of events with combined elastic and inelastic interactions is also shown. When searching for DES events, the whole background contribution must be taken into account [7].

are much more frequent than double elastic scatterings. Discriminating between inelastic and elastic collisions is crucial for the analysis of neutrons produced in PT, as is the possible mixing of the two populations. One possibility of discrimination is the neutron undergoing multiple interactions at a single vertex. Such an event would show multiple tracks at the same point, and would be discarded by the analysis. Further techniques of selection will be discussed in Chapter 4.

3.4.2 Recoiled protons and DES performances

A correct reconstruction of the neutron momentum requires the recoil protons to be fully contained inside the detector. The containment limit can be directly imposed on the Monte Carlo, requiring that a secondary proton is created and brought to rest inside the detector geometry. This constraint limits drastically the number of good DES events at energies above 150 MeV; as can be seen from Figure 3.10, the probability of such an event decreases of an order of magnitude.

For a correct modelling of the detector, the expected range of recoil protons can be estimated by studying their kinetic energy spectrum. Protons produced in interactions with monochromatic neutrons of energy 100 MeV result in Figure 3.11, where the distribution obtained with single elastic scatterings (black) is superimposed on the distribution of the first protons (green) and second protons (orange) scattered in a DES interaction. The constraints are that only protons crossing at least 3 layers of fibers that are also fully contained are considered. As expected, protons coming from SES have a uniform energy distribution from 12 MeV (corresponding to the minimum range of 6 fibers) to the primary neutron energy. For DES interactions, the first proton is forced to have kinetic energy less than the maximal energy available, in order for the neutron to undergo a second scattering, so it stops roughly at 80 MeV, also showing a slightly decreasing trend at higher energies. Therefore, the

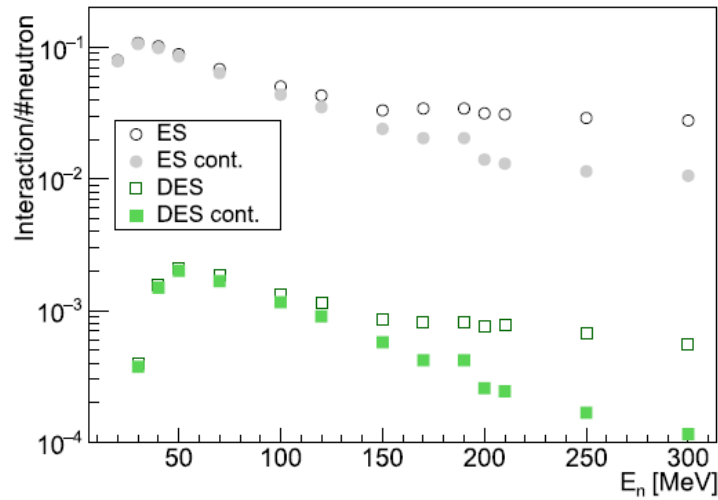


Figure 3.10. Expected number of interactions per incident neutron compared with the request of an event fully contained inside the detector. After 100 MeV, secondary protons are produced with energies high enough that their range goes out of the detection volume [7].

protons detected in MONDO will have energies in a range covering approximately the entire primary neutron range, expected to be 20 to 400 MeV.

DES simulations have given first estimates in 2019 [8]. Figure 3.12 reports preliminary results on energy and backpointing resolution, defined as the capability to distinguish between neutrons coming from the patient and those from the environment. As before, neutrons are sent into the tracker in monochromatic beams with known line of flight; proton energies are reconstructed from their range by fitting with NIST energy-range values, and their direction is determined by a linear fit to the proton track. The same considerations about the second proton track length from the SES reconstruction apply: longer tracks result in better accuracy. Results of reconstructed DES are compared with those obtained using proton energies coming

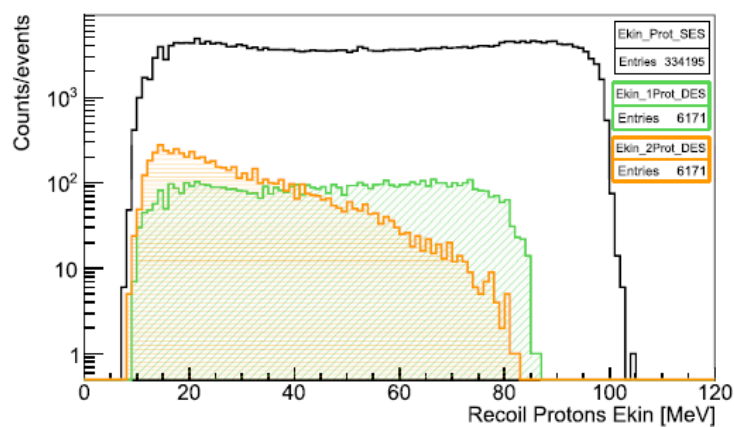


Figure 3.11. Kinetic energy spectrum of recoil protons produced by 100 MeV neutrons [7].

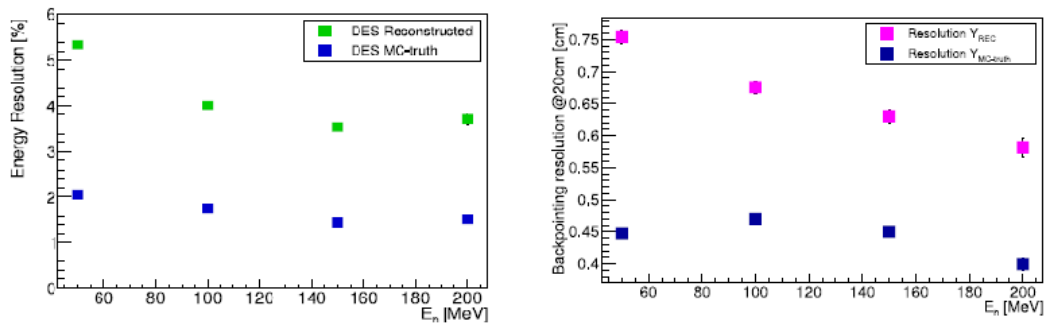


Figure 3.12. (Left) Energy resolution for reconstruction with DES interactions as function of the neutron kinetic energy. (Right) Backpointing resolution as function of the neutron kinetic energy. Error bars account for the statistical contribution in the energy measurement [8].

from Monte Carlo (MC truth). The average relative energy resolution has been evaluated to be in the range of 3.5%-5.5%, generally better than that estimated in the SES case.

Backpointing resolution depends on the distance and positioning of the detector with respect to the neutron direction. For the simulation, the neutron source is placed at a distance of 20 cm from the tracker. The achievable resolution is better than 1 cm without using MC truth energies, and increases with the primary neutron energy, as the linear fit to determine proton angles gives better results with longer, straighter tracks.

Chapter 4

Event reconstruction algorithm

This chapter will illustrate some conclusions taken from the analysis of neutron interactions with the MONDO texture simulated by means of the FLUKA Monte Carlo code. The simulation was conducted by sending monochromatic neutrons in the energy range of 30-450 MeV coming from a distance of 20 cm from the detector volume. The tracker geometry was built according to the disposition of fibers in the MONDO project, thus the passage of a particle is observed in two orthogonal x-y planes. The output data are stored in a ROOT file to be interpreted with a dedicated algorithm, written in C++ by the author of the present thesis work, equipped with information on detector geometry and a trigger selection method. The algorithm reads through every event, extracts the useful information, makes computations and, in addition to this, contains a display function able to produce a graphic picture of a single event as viewed by the switching on of the tracker pixels.

It needs to be emphasised that, so far, hardware components were only approximately taken into account in estimates of the tracker efficiency and resolution. An important requirement for this thesis work, and a fundamental difference with methods employed in the previous chapter, is that only quantities observable by the system readout output are exploited for the reconstruction, such as the activated pixels topology and the SPADs signal, and Monte Carlo truth is only used for comparison to prove the effectiveness of the implemented techniques.

The first task of the algorithm is to compute the occurrence of double elastic scattering (DES) events observable by the detector at a given neutron energy with the appropriate criteria of reconstruction capability. The number of such computed Monte Carlo DES constitutes the statistical population to be reconstructed from the observation variables. As it has been emphasised in Chapter 3, being able to distinguish between the intrinsic background of inelastic interactions and the interesting events is of fundamental importance. Topology and energy considerations come at help and the algorithm contains methods of discrimination which will be illustrated in detail.

The main way to interpret the passage of a charged particle through the detector is the formation of a cluster of triggered pixels, usually in the shape of a straight line. The algorithm is able to build a cluster based on the event topology, select those with the appropriate characteristics to be used in analysis (such as length and position with respect to each other) and, starting from two clusters in x and y

planes, construct a three-dimensional track candidate, which is the main object for the event reconstruction. Measuring the track candidate range and direction, the neutron kinematical variables are finally estimated. The final plots are resolution and efficiency plots: in particular, reconstructed neutron energy resolution, backpointing rejection capability and efficiency on reconstruction and selection of DES events.

4.1 Detector geometry and event study

The chosen sources of radiation are monoenergetic neutrons simulated impacting the detector on a straight line corresponding to the z axis of the MONDO tracker. The materials set by FLUKA are those of the active volume, that is the matrix of scintillating fiber planes, surrounding air and the silicon based readout system. The dimension of the tracker is set at $16 \times 16 \times 20 \text{ cm}^3$. It is embedded in a volume of air 10^3 m^3 large. For each energy, 3×10^6 neutrons are fired, and those that undergo some kind of interaction fill an event in the ROOT file; the analysis requires the storage of a great deal of information, including the type of every particle produced by the neutron interacting with the medium, its initial and final momentum, its production and absorption vertices, the pixels activated by its passage etc. In the next subsection it will be shown how an event is classified and the parametrization of the geometry.

```

*****
*   Row   * Instance *   nump *   idpa *   jpa *   igen *   tempo * (sqrt(px* *
*****
*       2 *       0 *   11 *       0 *       8 *   1000 *       0 * 100.00000 *
*       2 *       1 *   11 *       1 *      -6 *       0 * 2.410e-09 * 2.6999821 *
*       2 *       2 *   11 *       1 *      -6 *       0 * 2.410e-09 * 0.9729730 *
*       2 *       3 *   11 *       1 *      -6 *       0 * 2.410e-09 * 0.3534075 *
*       2 *       4 *   11 *       1 *       8 *   1000 * 2.412e-09 * 88.223529 *
*       2 *       5 *   11 *       5 *      -4 *       0 * 3.126e-09 * 7.2943974 *
*       2 *       6 *   11 *       5 *      -4 *       0 * 3.125e-09 * 8.0946580 *
*       2 *       7 *   11 *       5 *      -6 *       0 * 3.124e-09 * 6.8235173 *
*       2 *       8 *   11 *       5 *       1 *       0 * 3.127e-09 * 7.5413332 *
*       2 *       9 *   11 *       5 *       1 *       0 * 3.124e-09 * 2.1530836 *
*       2 *      10 *   11 *       5 *       8 *       0 * 3.126e-09 * 6.1139438 *
*****

```

Figure 4.1. An inelastic event (**igen**=1000) saved as an array of flags, taken from the simulation of a monoenergetic neutron at 100 MeV. Rows correspond to a particle, the values of **jpa** and **idpa** label the type of particle and its generation.

4.1.1 Detector geometry

The detector geometry source code contains the number of fibers and planes considered in the experiment. In the 3D space of the simulation, the origin of the axis is put at the center of the first x-y plane encountered by the neutron, as it is shown in Figure 4.2. Planes proceed to overlay one on top of each other along the z axis, with alternate x and y orientation. Each pixel occupies a rectangular spot on the faces of the solid. The simulation stores the position of an activated pixel, the number of photoelectrons collected by its SPADs, and the ID of the particle that caused the signal.

The trigger threshold for pixels, defined as the minimum number of fired SPADs in a pixel to start acquisition, is set at 3 for both views. Since the sensor architecture

is also implemented, the sensor trigger is analogously set at 3 pixels. These values have not been modified in the present work, and have been taken from a previous optimisation, but further studies on the sensor trigger to study the sensor geometry and efficiency are on the works.

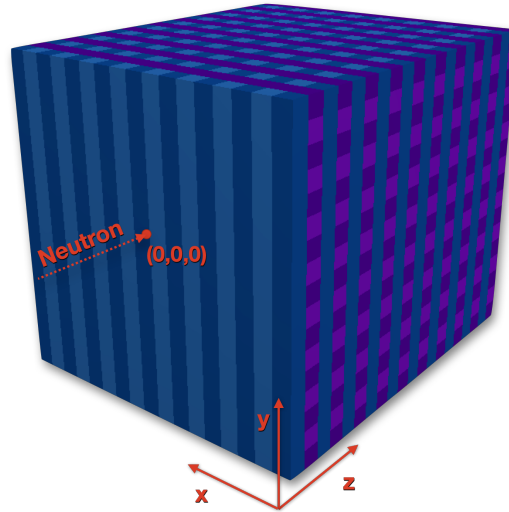


Figure 4.2. The neutron track impinging on the MONDO virtual geometry, with reference coordinates in the 3D space.

Because the neutron enters the detector in a straight line along the z direction, its initial four-momentum is completely known *a priori*. Generally speaking, a method for estimating the direction reconstruction efficacy can be reduced to a problem of determining the Closest Point of Approach (CPA), defined as the position at which two dynamically moving objects reach the closest possible distance. If one assumes to have reconstructed the direction of the neutron, the method is to trace back the neutron, reversing the time of its path outside the detector, and compute the point on a line passing through the origin where the reconstructed path reaches the minimum distance. If the direction reconstruction works well, the distribution of the coordinates of the CPA should have a peak corresponding to the coordinates of the source.

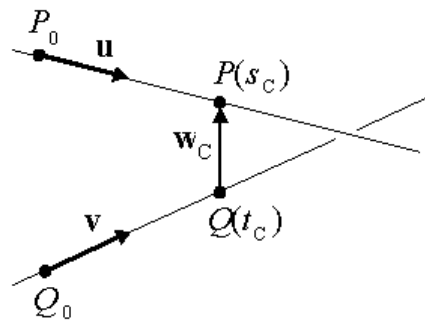


Figure 4.3. Calculation of CPA for backpointing reconstruction.

In formulas, consider two lines \mathbf{L}_1 and \mathbf{L}_2 of vector equation $\vec{P}(s) = \vec{P}_0 + s\vec{u}$ and

$\vec{Q}(t) = \vec{Q}_0 + t\vec{v}$, and let $\vec{w}(s, t) = \vec{P}(s) - \vec{Q}(t)$ be a vector between points on the two lines. The problem is to find the two points for which $\vec{w}(s, t)$ has the minimum length for all s and t . In any n -dimensional space, such a minimum is unique. Call it $\vec{w}_C = \vec{w}(s_C, t_C) = \vec{P}_C - \vec{Q}_C = \vec{P}(s_C) - \vec{Q}(t_C)$; the further property to be exploited is that, if the two lines are not parallel and do not intersect with each other, \vec{w}_C has the unique property among all vectors joining the two lines, to be simultaneously perpendicular to both \mathbf{L}_1 and \mathbf{L}_2 , so $\vec{u} \cdot \vec{w}_C = 0$ and $\vec{v} \cdot \vec{w}_C = 0$. Solve the equation by substituting $\vec{w}_C = \vec{w}_0 + s_C\vec{u} - t_C\vec{v}$, where $\vec{w}_0 = \vec{P}_0 - \vec{Q}_0$, and get:

$$\begin{aligned} (\vec{u} \cdot \vec{u})s_C - (\vec{u} \cdot \vec{v})t_C &= -\vec{u} \cdot \vec{w}_0 \\ (\vec{v} \cdot \vec{u})s_C - (\vec{v} \cdot \vec{v})t_C &= -\vec{v} \cdot \vec{w}_0 \end{aligned} \quad (4.1)$$

Calling $a = \vec{u} \cdot \vec{u}$, $b = \vec{u} \cdot \vec{v}$, $c = \vec{v} \cdot \vec{v}$, $d = \vec{u} \cdot \vec{w}_0$ and $e = \vec{v} \cdot \vec{w}_0$, the following solutions for s_C and t_C are obtained:

$$s_C = \frac{be - cd}{ac - b^2} \quad \text{and} \quad t_C = \frac{ae - bd}{ac - b^2}.$$

4.1.2 Event classification

As an event takes place, the particle and pixel parameters are saved inside a vector of variable size. This includes the particle time and place of creation/scattering, its momentum and its time of flight. Since the MC analysis is interested first and foremost on protons, a flag is given to unambiguously label particles of different types¹ present in the interaction. This way it is known exactly how many recoil protons, electrons, photons, ions and so on are present at any moment in the interaction.

It is then important to label the type of interaction that takes place. Elastic scattering interactions used for the reconstruction of the neutron kinematics have to be distinguished from a background of inelastic processes such as nuclear fragmentation and recombination, in which the kinetic energy of the original neutron is not uniformly distributed among reaction products. For this purpose, an increasing number, from 1 to n , counts how many elastic interactions with protons the neutron has gone through, whilst an inelastic event is labeled with the number 1000. A combination of elastic-inelastic is obtained by summing the number of elastic interactions to 1000.

Finally, the analysis needs to distinguish between particles which come from an interaction with the primary beam (secondaries) from others produced through successive interactions of the scattered products with the medium (tertiaries etc.). A flag going from 0 to n is set for this aim, 0 corresponding to the primary neutron and n to a particle of the n -th generation.

Since the energy reconstruction depends on a relation with the particle range, the Monte Carlo kinetic energy of each particle is extracted from the momentum by the relation:

$$E_{kin} = \sqrt{m^2c^4 + p^2c^2} - mc^2 \quad (4.2)$$

and the range is computed from the points of beginning and end of path of the particle. The particle is flagged as contained inside the detector if it comes to rest

¹See www.fluka.org for a complete list of codes and labels.

inside the active volume. This analysis has considered the following processes as good approximation of an experimental situation where one can observe particle tracks moving across the detector:

- a charged particle with a confidence path of 2 mm, corresponding to a proton energy of 10 – 12 MeV and to 3 activated pixels in both tracker views (e.g. minimum number of fibers for tracking), is considered as valid candidate of reconstruction. The vast majority of such particles are protons, with light ions and pions contribution raising at higher neutron energy (see Figure 4.4 Left);
- if the neutron produces only one secondary particle, satisfying the requirement above, and the interaction was elastic, the event is labeled as *single elastic scattering*; if secondaries are more than one, and the first two produced in chronological order are protons coming from elastic interactions, the event is labeled as *double elastic scattering*;
- if the particle activating pixels is not a recoil secondary proton, the event is labeled *single not-SES*; if there are at least two particles able to produce a detectable signal, the event is flagged as *double not-DES*.

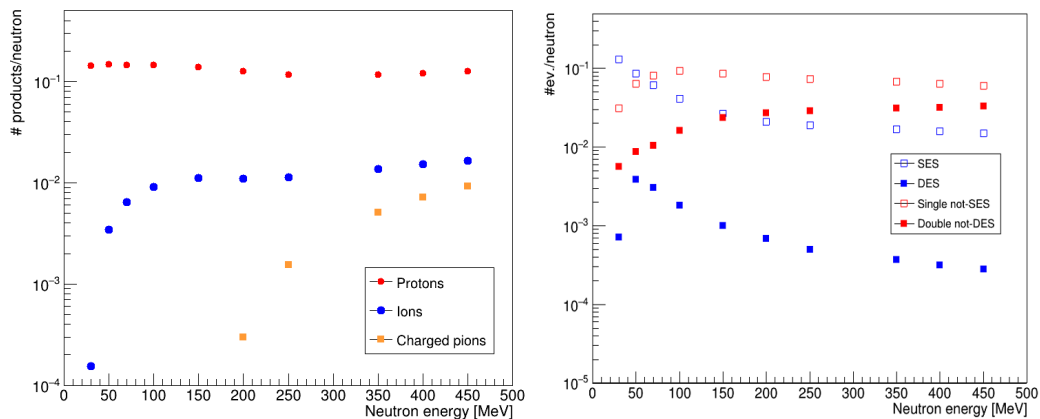


Figure 4.4. (Left) Number of charged products of interaction per neutron with range inside MONDO > 2 mm. (Right) Number of different interactions per neutron impacting on the detector.

Single elastic scatterings (SES) are the simplest processes to study and are used as reference to find analysis tools with topological criteria to distinguish them from inelastic events, that can then be transferred in the double elastic case. To test the flags, a plot showing the rate of single and double elastic events as function of E_n is shown in Figure 4.4 (Right), calculated for the ionizing particles fully contained inside MONDO with range > 2 mm. It has been found that the graph obtained with the above constraints is in substantial agreement with the results of the precedent simulation ([8]), with SES events being dominating at energies below 100 MeV and double elastic scatterings reaching a peak at about 50 MeV.

The rate of double not-DES events is higher due to the fact that, in this case, the counting comprises any event with two triggering particles not being the first two

elastic recoil protons, thus including events where an intermediate elastic interaction may have not been reconstructed and/or the neutron scatters elastically against other kinds of particles, such as carbon ions. It shall be seen in the next sections that with appropriate reconstruction considerations and the development of a rejection algorithm, the rate of reconstructed inelastic events at energies lower than 150 MeV can be drastically reduced.

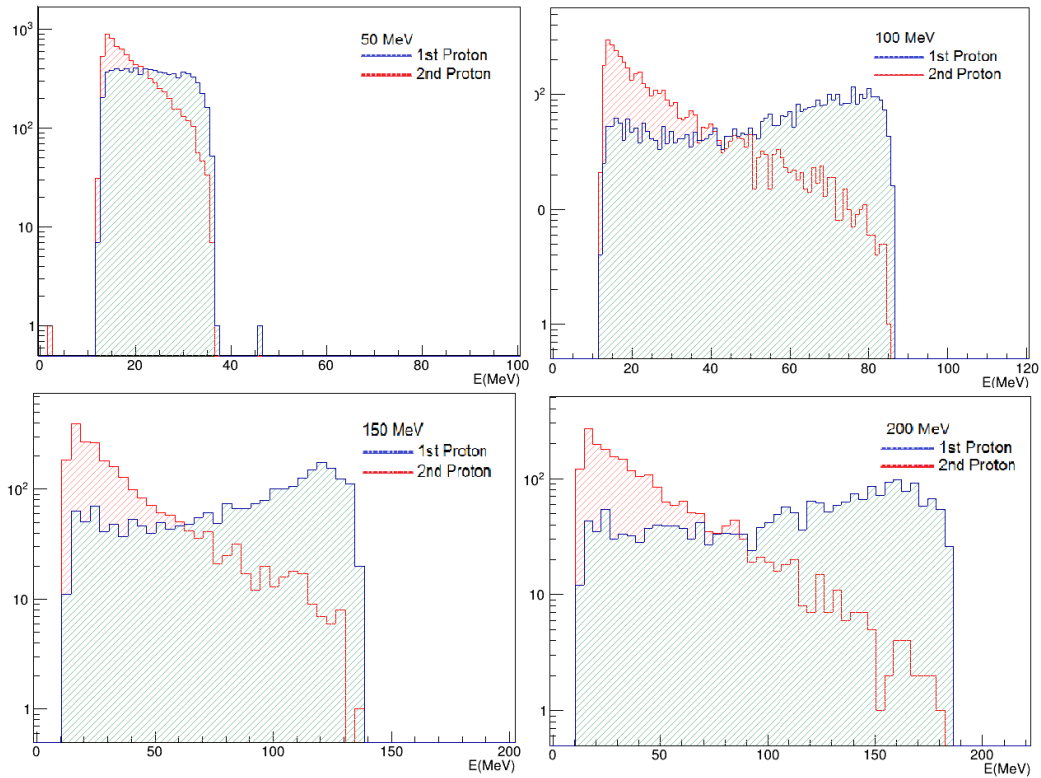


Figure 4.5. Compared kinetic energy spectra for double elastic scattering recoil protons, at 4 different initial neutron energies. The run at 100 MeV can be compared with Figure 3.11. The others show a similar trend in the distribution, roughly uniform for the first proton and with a peak at low energies for the second.

The expected distribution in energy and range of the two recoil protons for a DES event has also been obtained, and it is shown in Figure 4.5. Four distributions of the proton energies are compared, at initial E_n of 50, 100, 150 and 200 MeV. The expected requirement that the first proton kinetic energy reaches a maximum value lower than the full transferable amount is fully satisfied, as is the observance of the peak at lower energies for the second, less energetic recoil proton.

4.1.3 Event display

As part of the reconstruction algorithm, a function of event display has been developed, with an interactive and intuitive interface for the user. In the Figure 4.6 an example of DES event is shown. From the point of view of the image, the two directions of reconstruction are shown as different 2D planes; for each event, the

canvas is filled with the activated pixels, with a color scale based on the number of SPADs. It is possible to navigate through events with clickers, or by inserting the number of a specific event inside the box to directly access it. The type of interaction (based on the flags previously established), the number of triggered pixels in both planes and the trigger flag are indicated.

Events can be zoomed, for example highlighting the presence of a Bragg peak (see Figure 4.7 Left), and can be used to visualize the topology of events that need to be excluded from the process of reconstruction, like the clearly not-contained events or the typical inelastic multiple-tracks events, where more than one particle track departs from the interaction vertex, as shown in Figure 4.7 (Right). The other feature that appears is a function that allows the user to see the event in terms of clusters instead of individual pixels, and two counters of the number of clusters present on each side. How a cluster is built and what is its role in reconstruction will be discussed in the next section.

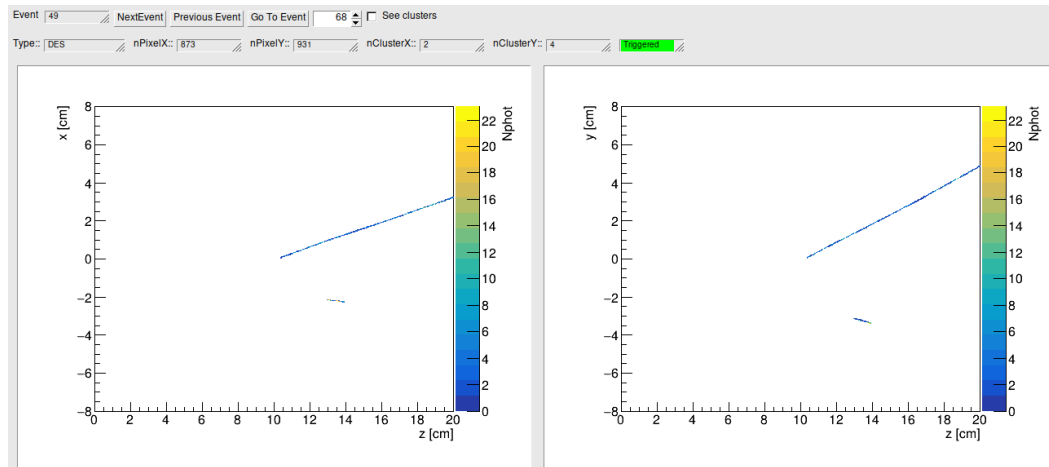


Figure 4.6. An event display of a DES event. Since the cluster ends at the border of the detector, it can be concluded that the event is not contained.

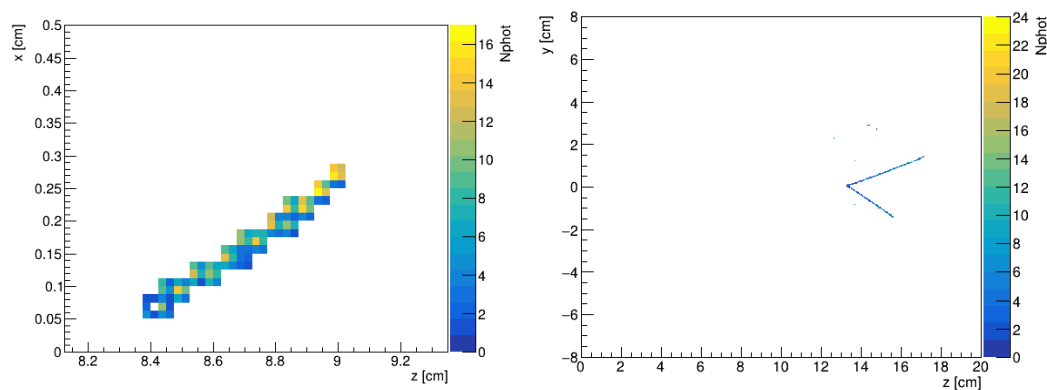


Figure 4.7. (Left) An expanded view of a group of pixels showing a high number of photo-electrons at one side of the path, strongly suggesting the presence of a Bragg peak. (Right) Display of an inelastic event with a multitrack vertex.

4.2 Clusters and Tracks

This section describes how clusters are assembled, their characteristics as function of the neutron energy, and their comparison with Monte Carlo data. After that, they are further assembled into 3D track candidates, that are used for energy and direction reconstruction of the recoil protons. All the selections that have been decided to clean the analysis from spurious events like inelastic scattering and not-contained particles, what effects these cuts have on the number of reconstructed protons and how the Monte Carlo data are reproduced according to these assumptions will be discussed in detail.

4.2.1 Clusters building and analysis

The cluster is prepared by starting a cycle on the activated pixels of the event. Two separate processes are run for x and y planes. The cluster building code first flags all pixels with a “not-yet-assigned” variable, then starts a loop on their set, choosing as seed the first element of the cycle, and adding further pixels as long as the distance between them is less than 0.75 mm; the process is thus interrupted if there are more than two blanks between pixels, and the code begins building a new cluster, and continues assembling until every activated pixel is assigned to a cluster.

With the finished structure, three variables need to be set:

- the assignment to the passage of a particle, that is achieved by Monte Carlo looping on the constituent pixels, each of which have a unique particle ID, and getting the most frequent value;
- the direction that needs to be compared with the projection of the particle path on the cluster plane, which is set by taking the pixel with the z coordinate closest to $z = 0$, and the farthest, and tracing a line between them;
- the verse along the z axis, forward or backward with respect to the positive direction, computed supposing that the pixel with the maximum number of SPADs in the cluster, that corresponds to the highest release of energy, resides in the Bragg peak zone, near the end point.

The distance of the two pixels at the extremes of the direction segment with the Bragg Peak is checked: the closest is defined as the end pixel, the farthest as the starting pixel. The cluster can thus be thought as a vector of coordinates $(x_{max}^x - x_{min}^x, 0, z_{max}^x - z_{min}^x)$ if it belongs to the x plane, and $(0, y_{max}^y - y_{min}^y, z_{max}^x - z_{min}^x)$ if it lays into the other. This method of approximating a cluster to a line is quite crude, but it gives reasonable comparison with Monte Carlo data for range and energy.

A dispersion plot with the Monte Carlo results is shown for ranges in the single elastic case, since this is the easiest to treat. The recoil proton has the usual constraints of having a range greater than 2 mm and being contained inside the detector. As can be seen from the plots in Figure 4.8, obtained with neutrons at 100 MeV and 200 MeV, the projection of the particle track on the plane is linearly reproduced by the cluster.

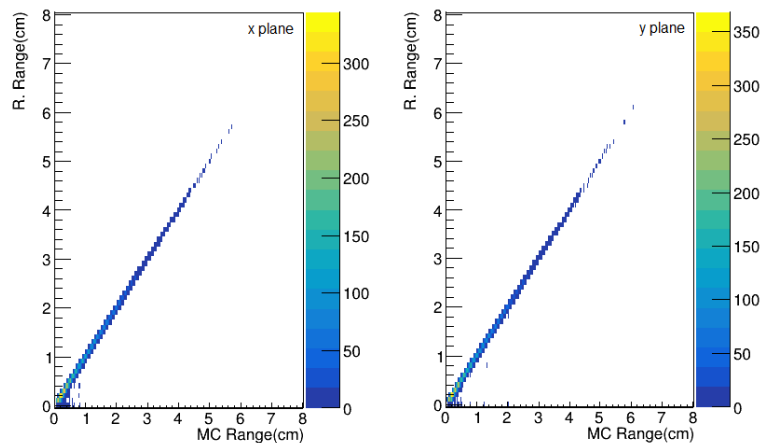


Figure 4.8. Dispersion plot of cluster length with the projection on plane x/y of the Monte Carlo SES proton direction.

From the plot of the cluster size as function of the particle energy (taken from Monte Carlo) in Figure 4.9, it is possible to conclude to what extent the cut applies to the number of pixels. In fact, only particles with $E_{kin} > 12$ MeV are reconstructed, based on the condition imposed on the minimum range, and this corresponds to a minimum cluster size of about 28 pixels, under which value no object with the required characteristics is found. Thus, when putting together DES events, it is safe to impose this limit to get rid of non-reconstructable particles.

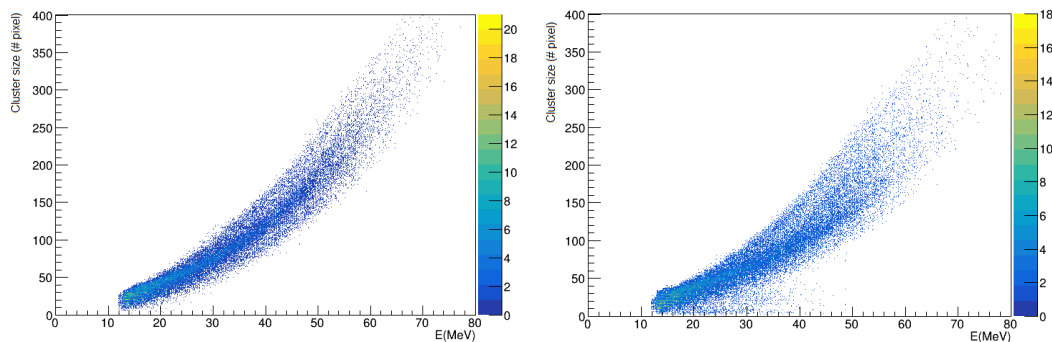


Figure 4.9. Scatter plot of the number of pixels of the cluster as function of the Monte Carlo energy of the particle associated to it by the algorithm assignment. (Left) $E_n = 100$ MeV. (Right) $E_n = 200$ MeV.

The method of cluster building gives reasonable results in the case of SES events at energies lower than 100 MeV; however, problems are encountered as the initial neutron energy increases. In particular, inelastic interactions can give rise to an incorrect estimate of the range and energy of the particle due to a cluster building not taking into account the presence of peculiar shapes like the ones in Figure 4.10.

On the left is a discontinued track, due to the limited granularity of the apparatus, and on the right is the already encountered V-shape multitrack inelastic interaction, that is however reconstructed as a single cluster. The linear approximation is inapplicable in this case. This feature could be used to have a preliminary factor of

discrimination against inelastic events, through the definition of a parameter which, based on the range of values, establishes if the process is elastic or inelastic.

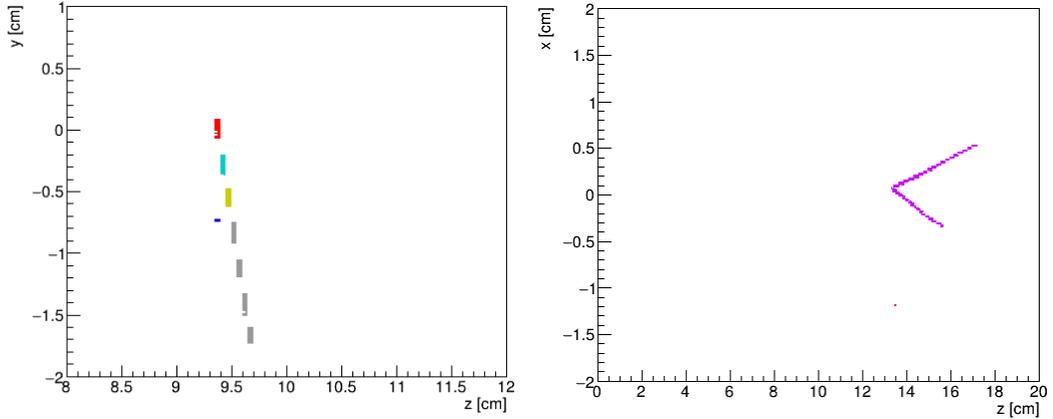


Figure 4.10. (Left) A disconnected proton track. Every step is treated by the code as a separate cluster, resulting on an overestimate on the number of particles, all with short range. (Right) A multitrack vertex event where a single cluster is built out of the pixels activated by different particles.

During this thesis work, an estimate has proven successful at least against V-shaped events. To compute it, consider a single cluster, and trace a line from the pixel with the minimum z to the one with the maximum z . Then make the distribution of the distance of each pixel from this line (the orange segments in Figure 4.11), and take its standard deviation. In Figure 4.12 the result of this parameter, called σ , for SES and purely inelastic events is shown, for $E_n = 100$ MeV. By cutting at $\sigma \simeq 0.02$, the large tail of anelastic events is excluded from reconstruction. For values closer to 0, however, where the two distributions are both present, a different argument is needed, and will be discussed in the next section about DES event reconstruction.

4.2.2 Track candidates building

The next objective is to bring the analysis to the three dimensions, a necessary condition for the full neutron four-momentum reconstruction. The 3D object which is assumed to contain the information about the passage of a particle is called *track candidate*. The code builds a track candidate by joining together two clusters, one in the x-plane and the other in the y-plane, based on the following criteria:

- the two clusters must both have dimension greater than or equal to 28 pixel, for reasons we have illustrated in the cluster section;
- in the respective planes, they must start and end at the same depth, so the initial and final z must correspond, with a confidence interval of 1 mm;
- there should be no ambiguity in joining together two clusters on opposite views; so, for example, if two clusters start and end on the same z in the same view, with the same confidence interval of 1 mm, a one-to-one correspondance with a cluster on the opposite side cannot be established, and they are both

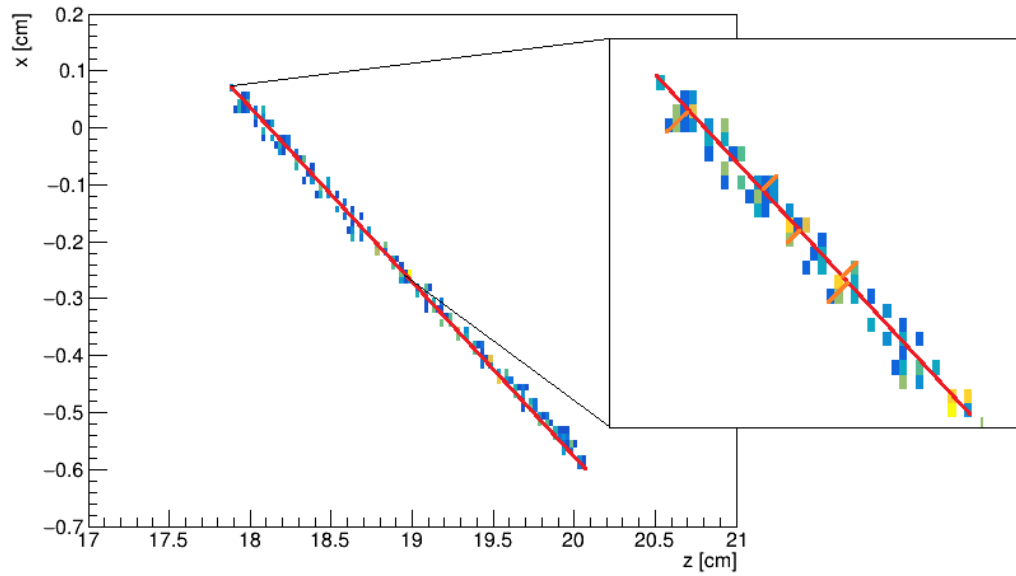


Figure 4.11. Method of computing a parameter for the shape discrimination of the cluster. The red line indicates the reconstructed trajectory along the x plane. The orange segments represent the distances of each pixel from the direction line.

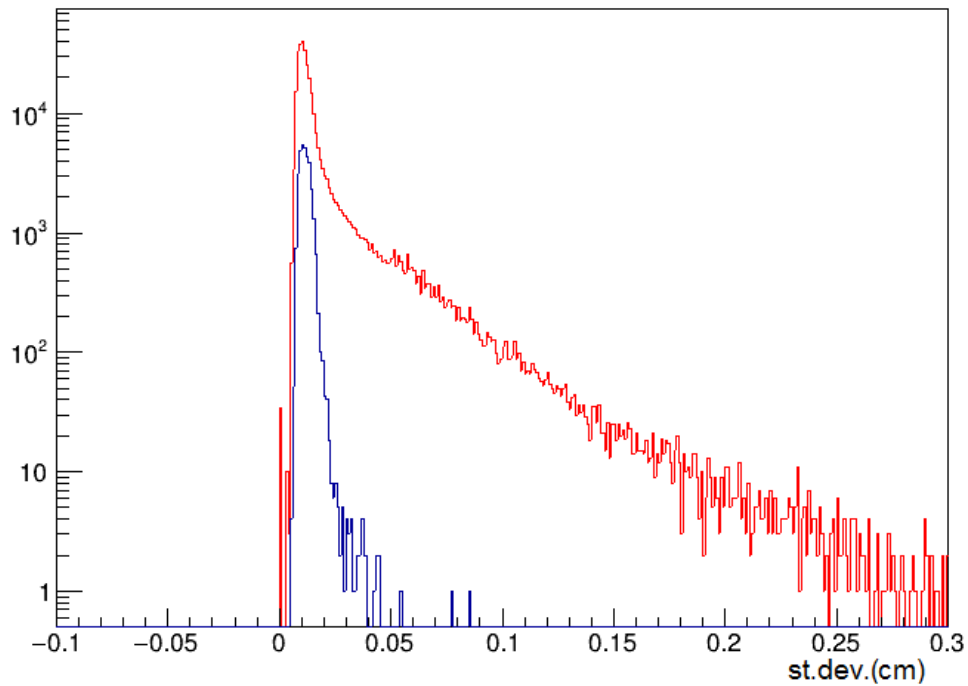


Figure 4.12. Value of standard deviation from the reconstructed direction for every cluster built per event, at neutron energy of 100 MeV. Clusters of minimum dimension of 28 pixels are considered. The population in red are clusters produced by products of inelastic interactions, in blue by single elastic scattering recoil protons. The inelastic tail is put in evidence by the logarithmic scale.

taken out of the analysis. It is safe to say, and has been verified, that such an eventuality occurs most often to small, pointlike clusters, that are already mostly discarded by the first condition, and does not affect sensibly the final number of track candidates.

When all the three conditions apply, a track candidate is created by the algorithm. As for the cluster case, a track candidate range and direction is obtained by taking the coordinates of a minimum and a maximum along the z axis; the x and y coordinates are directly taken from the proper cluster (so $x_{max} = x_{max}^x$, $y_{max} = y_{max}^y$, and so on), whilst for the z coordinate an average is taken:

$$\begin{aligned} z_{min} &= \frac{z_{min}^x + z_{min}^y}{2} \\ z_{max} &= \frac{z_{max}^x + z_{max}^y}{2} \end{aligned} \quad (4.3)$$

where z^x and z^y refer to coordinates on planes x and y respectively. The track is thus treated for the purpose of reconstruction as a vector pointing in the particle direction of motion of coordinates $(x_{max} - x_{min}, y_{max} - y_{min}, z_{max} - z_{min})$.

4.2.3 Direction method and analysis

One thing to be emphasised is that the Monte Carlo comparison could fail to apply in certain cases where it is not possible to assign univocally a track candidate to an interaction particle; while clusters are uniquely associated to a particle through a counting method, the algorithm could erroneously link two clusters belonging to different objects in a track, which would result in not having a definite particle flag. For this reason, the percentage of tracks correctly associated to a single entity has been constantly checked to be more than 90%. Not only this, but because multitrack events are inserted into track candidates as unique clusters, anelastic events does not have an obvious link to Monte Carlo properties. Consider, for example, the plots on Figures 4.13; they are obtained taking the unitary vectors along the directions of the track and of the particle MC truth (when it is possible to link the two by a unique particle ID) and making the difference between them, along the x , y and z coordinates:

$$D_i = (\hat{n}_{\text{track}} - \hat{n}_{\text{MC}})_i \quad i=x, y, z$$

While the differences in x and y show a peak at zero and symmetric tails, the difference in the z direction is clearly different: the tail is asymmetric, indicating that the code has a surplus of instances where the particle is moving forward in the z direction, but it is reconstructed backwards. This could happen both if the particle is not contained, in which case the Bragg peak lies beyond the experimental volume, or because the track is made of clusters with few pixels, among which a clear Bragg peak cannot be identified. The fact that the backward reconstruction is favored could depend on inelastic effects happening at multitrack events, and is currently under investigation. Direction inaccuracy does not affect the energy reconstruction, but it can return as an undesired effect in the computation of angles between tracks.

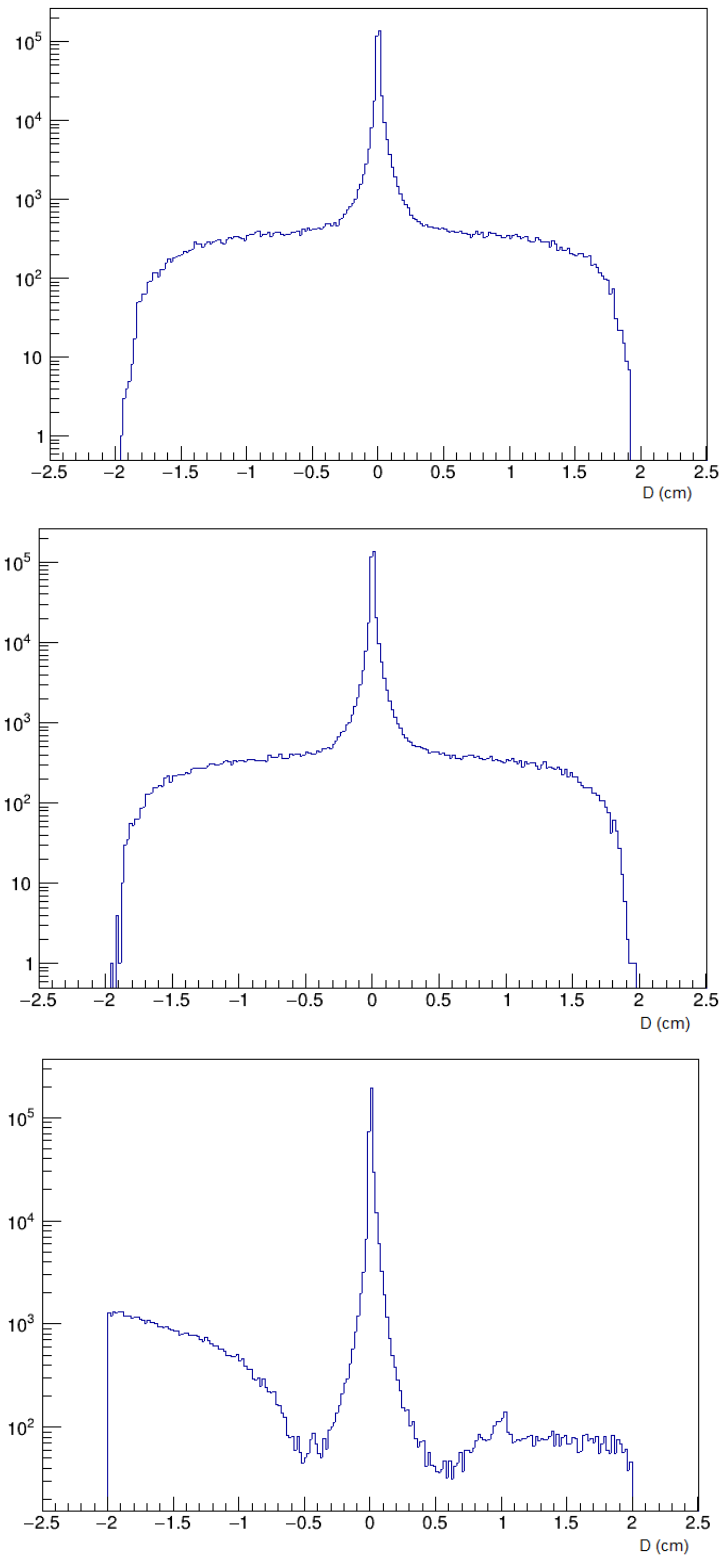


Figure 4.13. Plots showing a possible comparison of reconstructed directions with MC. The quantity plotted is the difference between 3D vectors along x , y and z . The difference between 3D vectors along z shows an asymmetry with an overpopulated negative half. It indicates that the code incorrectly reconstructs particles moving forward in the opposite direction more often than the contrary (backward/forward).

4.2.4 Range and containment study

The reconstructed particle range inside MONDO is taken as the modulus of the vector $(x_{max} - x_{min}, y_{max} - y_{min}, z_{max} - z_{min})$. A containment constraint is also introduced, to mirror the Monte Carlo requirement. Calling L_x , L_y and L_z the tracker edges corresponding to the 3D cartesian axes, the confidence volume is defined as the solid with the same center as MONDO with edges $L_x - 1$ mm, $L_y - 1$ mm and $L_z - 1$ mm. If both the track extremities are inside the confidence volume, the track is flagged as contained. A comparison between Monte Carlo and reconstruction to estimate the efficacy of the constraint has been carried out. The Figure 4.14 has been obtained taking every event and checking if containment is (un)satisfied by both the condition described above and the Monte Carlo value. The two agree more than 95% of the time at any energy considered, so the method is proved to be effective.

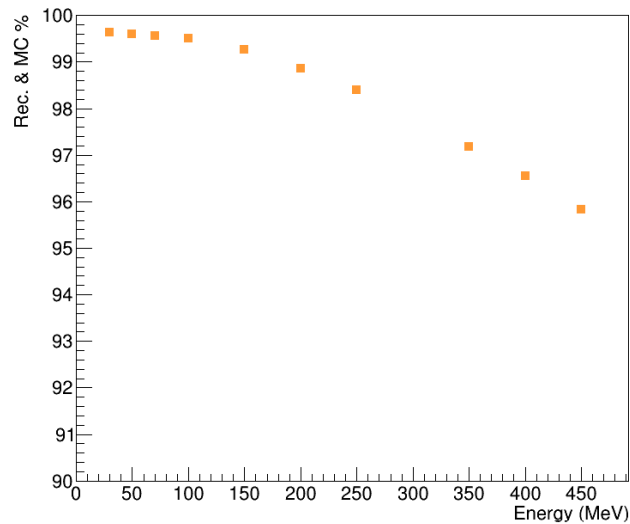


Figure 4.14. Percentage of events where at least one track is present and, given a confidence volume inside which the track is considered contained, the constraint coincides with the Monte Carlo result, so the event is (or is not) contained for both reconstruction and Monte Carlo truth.

The energy-range relation is usually given as a power function of two parameters:

$$R = \alpha E^p \quad (4.4)$$

where the parameters are extrapolated with values from www.nist.gov in the energy interval 10-250 MeV. The shape of the function has been represented with the track candidates range with E_n of 250 MeV, and the result is depicted in Figure 4.15. It gives also a justification for the requirement to reconstruct protons at energies above 12 MeV. Because the function tends to flatten near 10 MeV, there are many values of the range corresponding to a low value of energy, and the uncertainty is so large that it is always better to require longer proton tracks. In fact, in Chapter 3, the need for longer proton tracks to enhance resolution has been enforced multiple times.

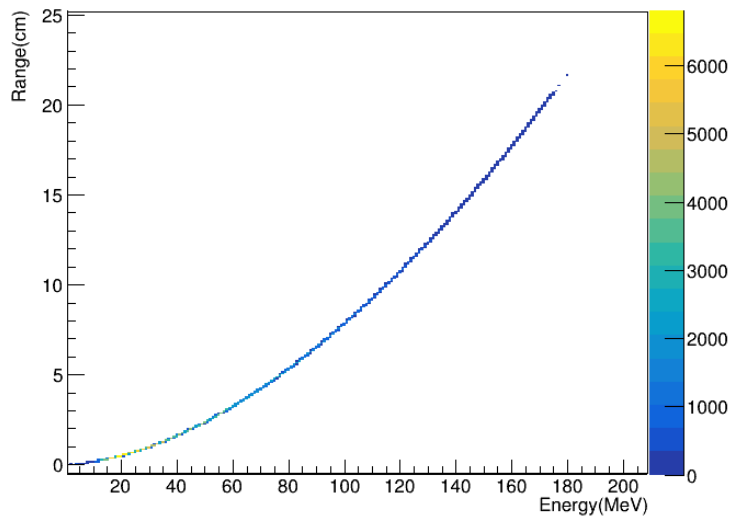


Figure 4.15. Reconstructed range of the tracks as function of Monte Carlo energy of the proton, done to show the fitted function with NIST values. Notice that, at energy lower than 10 MeV, the relation becomes unreliable because of the closedness of ranges at nearby energy values.

The range for single scattering protons is correctly computed; from the Figure 4.16 it is clear that anytime an elastic event is reconstructed, the computed range has a linear relation to the Monte Carlo length of the particle track. In the general case (Figure 4.17), including every track candidate built in the event, a number of instances where the range is overestimated is observed, on one side, and on the other a sparse population of the opposite case, with the range underestimated with respect to MC.

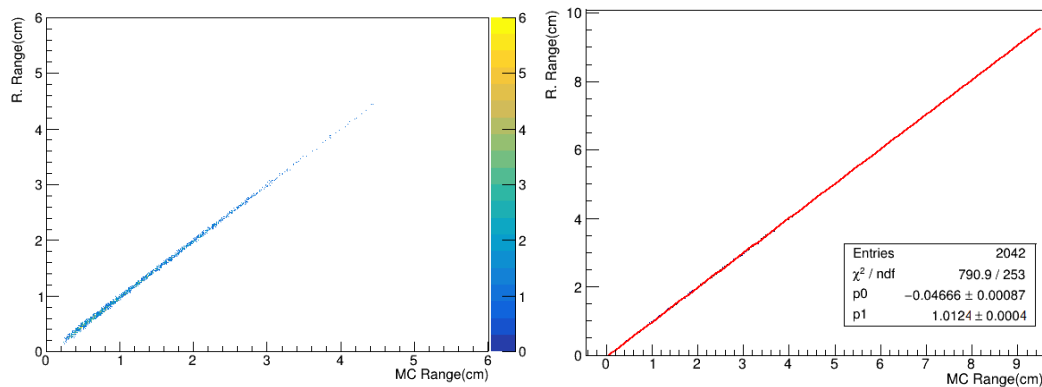


Figure 4.16. Track reconstructed range confronted with the respective Monte Carlo particle range, in the case of single elastic scattering at neutron kinetic energy 200 MeV. (Left) Dispersion plot. (Right) Linear fit on the plot profile. The locus of the points is the bisector of the plane.

The latter can be explained by the containment request, with some particles escaping the detector and the tracks not being correctly flagged due to intrinsic limit in the detector resolution, or to inelastic events where the proton has an

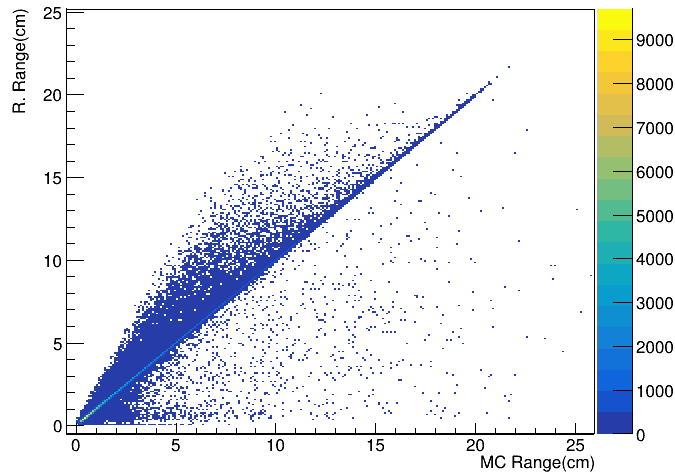


Figure 4.17. Dispersion plot of reconstructed range vs Monte Carlo truth. The linear relation is still visible, with the largest density of track candidates, however two more population arises: the locus of points under the bisector, which correspond to not-contained events and/or inelastic scatterings bending the particle track, and those above the bisector, which are due to multitrack vertices.

interaction that bends its trajectory, and the line joining together the two extremes is obviously smaller than the total path. The former is also caused mainly by inelastic interactions, particularly by multitrack vertexes events: since in this case the algorithm assigns every neighboring pixel to a single cluster, and to that cluster associates a unique particle flag, every particle exiting the vertex is reconstructed with the same range, which can be significantly larger than the correct one. A future analysis on multitrack events will be needed to take into account their impact on energy resolution.

4.2.5 Energy and hardware variables relations

To wrap up the discussion on track candidates, plots concerning the link to hardware variables and on the detection efficiency are drawn. Figure 4.18 shows on the left the dispersion plot for the number of photoelectrons produced through all the track candidate pixels as function of the energy of the traveling particle, in the case of single elastic scatterings. Notice once again the cut at 12 MeV and the gradient becoming higher with E , suggesting that the number of triggered SPADs, being a measure of the proton energy loss, is strongly correlated with the range of the particle. Finally, on the right, the number of SPADs is plotted against the number of pixels, again for SES protons; in this case, the cut is around 60 pixels, that is approximately 2 times 28, and the trend resembling that of the range-energy relation². This plot is important from the hardware point of view, since it contains how the experiment reproduces the range-energy parametrization of Eq. (4.4), and its investigation could reserve important results, that are planned for future steps of the reconstruction algorithm.

²Reversed, because SPADs are measure of energy, and pixels of range.

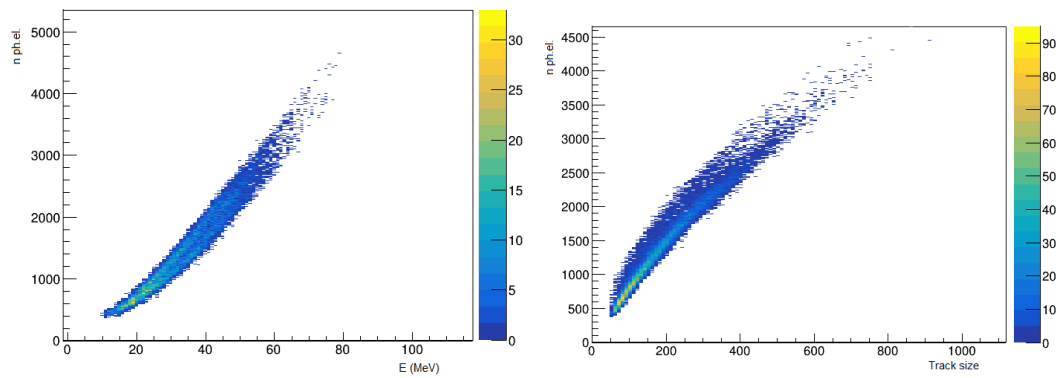


Figure 4.18. Dispersion plot taking into account the hardware variables. (Left) The number of fired SPADs per track as function of the energy of the SES proton. (Right) The number of fired SPADs per track as function of track candidate size in terms of pixels for SES events.

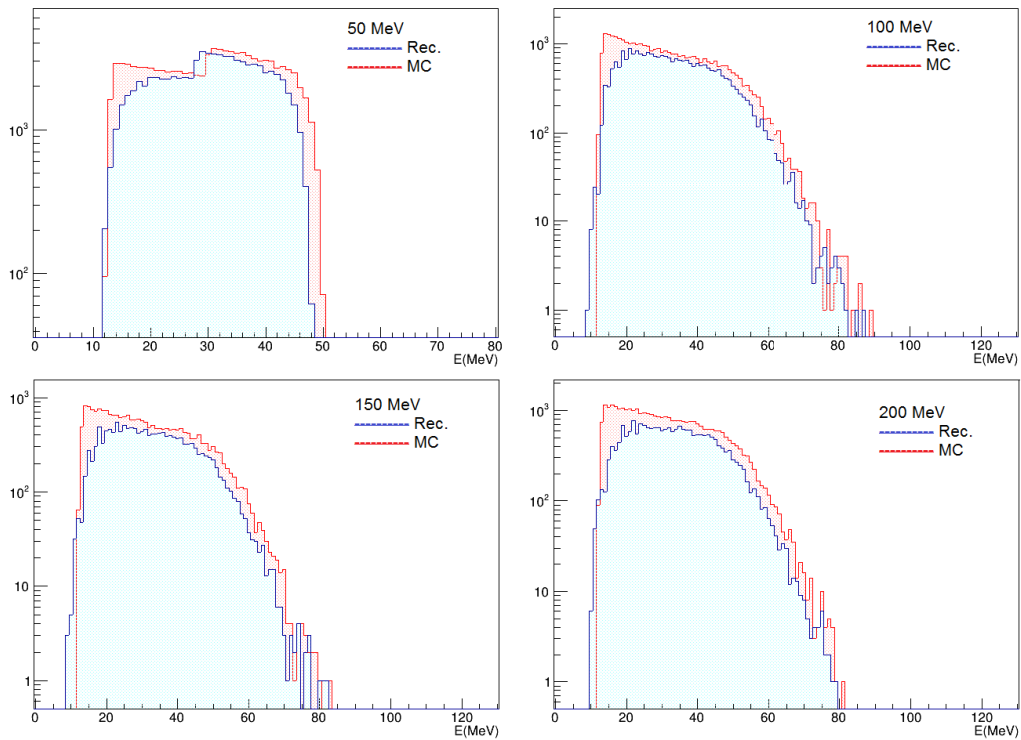


Figure 4.19. Reconstructed energies for contained protons produced by neutrons of different energies.

The plots in Figure 4.19 show the distribution of reconstructed proton energies in the case of single elastic scatterings, superimposed with the Monte Carlo distribution taken with the appropriate constraint of minimum range and containment. As expected, protons with energy greater than 80 MeV exit the detector, and, at the lower extreme, the largest fraction of detectable protons lost in the process of reconstruction are at energies around the cutting edge of 12 MeV. This reduces the detection capability for short tracks, and the effect becomes more important as E_n drops below 50 MeV (as an example, reconstruction of DES events at 30 MeV is shown in Appendix A).

4.3 DES events reconstruction

The elements to proceed with a first attempt at double elastic scattering reconstruction are available. For the sake of cleansing the analysis from spurious events, the restriction imposed for DES reconstruction consists in picking up only events where 2 and only 2 track candidates have been built by the algorithm. This way, one can imagine that the only particles present that give the tracker a fully exploitable signal are two protons. The other constraint is hardware containment, that is the two track candidates must have starting and ending points inside the confidence volume defined in Section 4.2. The results obtained limiting oneself to these restrictions are first presented, highlighting the need for an additional condition in order to minimize the contribution of inelastic interactions.

4.3.1 Energy

The names of the variables will be, referring to Figure 3.1, E_p , \vec{p}_p , E'_p and \vec{p}'_p the kinetic energies and momenta of the first and second recoil protons, θ and θ' the angles between the neutron and proton directions at the two vertices, \vec{p}_n and \vec{p}'_n the momenta of the incoming neutron and of the neutron scattered at the first vertex. The track starting at the earlier z is identified as the first proton track, the successive as the second. In Figure 4.20, the two reconstructed spectrum for E_p and E'_p are displayed for $E_n = 100$ MeV; it is worth noting that the first proton kinetic energy is much more peaked at lower energies than in the Monte Carlo plots. Moreover, the maximum value of E is closer to E_n , which is a clear indication that inelastic protons come into play.

To make this point clear, the analysis is carried on nevertheless, proceeding with the computation of θ' and E'_n . Taking the position of the two vertices as the path traveled by the diffused neutron, θ' is calculated as the angle between this line and the second proton track. E'_n is obtained applying Eq. (3.1), and E_n is simply $E_p + E'_n$ if the scattering is elastic. The resulting neutron energy for all the selected events had the distribution of Figure 4.21 (MC $E_n = 100$ MeV). The peak corresponding to 100 MeV is visible, together with a pronounced background and a second peak at about 80 MeV.

Since track candidates for elastic protons reproduce well Monte Carlo truth, double-track inelastic interactions distort the analysis and introduce a non negligible contribution to the reconstructed E_n . Taking advantage of the Monte Carlo, Figure 4.21 pictures the separate contribution of elastic and inelastic events to the

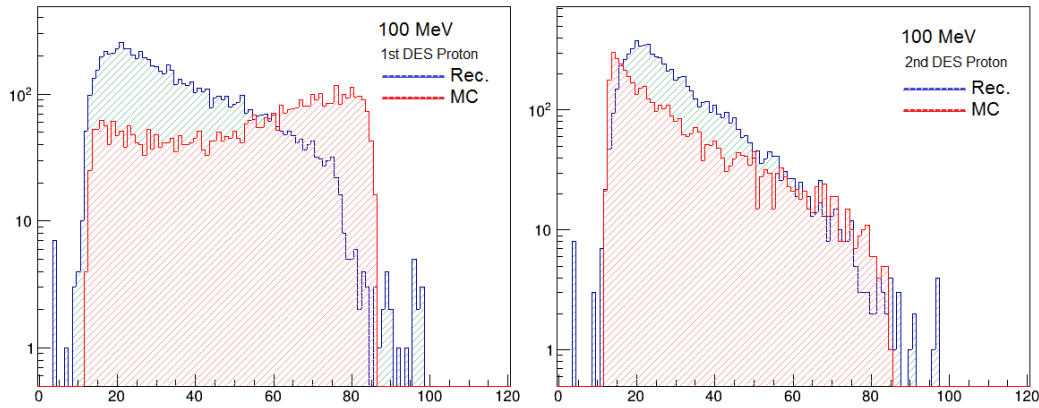


Figure 4.20. Reconstructed (blue) and MC truth (red) kinetic energies of protons in a DES candidate event (only two tracks detected, fully contained in the confidence volume).

total reconstructed kinetic energy, using the flags introduced in Section 4.1. The blue graph is obtained by taking all the events fully contained with two tracks, and counting how many of them are actually DES by Monte Carlo. Analogously, the red graph represents the purely inelastic interactions among those picked as DES candidates. It is evident that inelastic events account for the majority of the background and also for the double peak, the nature of which is currently under investigation. What is crucial is that reconstructed DES events are located precisely at the peak, so that when picking the right type of scattering, the code reconstructs the correct E_n .

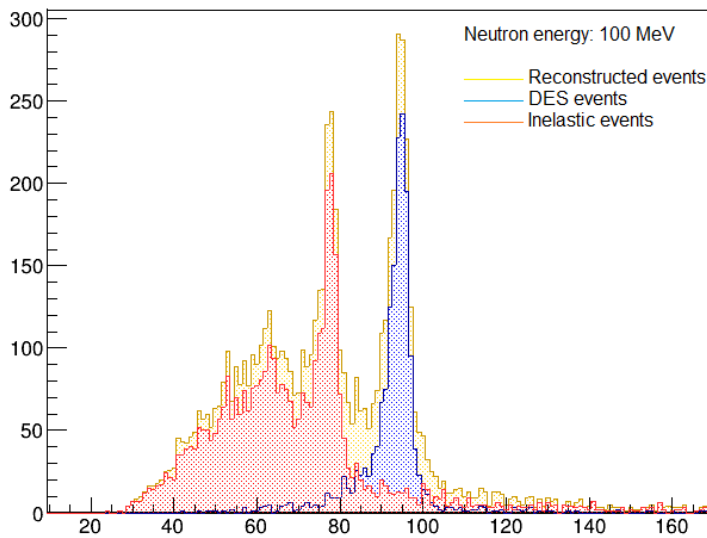


Figure 4.21. Separate contributions to the total reconstructed events without topology constraints. The whole population of DESs (blue) gives the correct peak. Inelastic events (red) account for the incorrect estimate region.

To the aim of evaluating the resolution on the neutron energy, the algorithm needs a function to keep good events and take out the inelastic component. To a

certain extent, this is the criterion that affects both resolution (how many incorrect instances it cuts) *and* efficiency (how many events with the correct reconstruction are kept) the most, and its efficacy is of fundamental importance.

The chosen criterion has been a geometric consideration: in the non-relativistic domain, elastic scatterings between two particles of equal mass, where one particle is at rest, obeys a kinematical condition on the angle between the two vector velocities of the outgoing objects. Since (calling v_p and v_n the proton and neutron velocities) $\vec{p}_n = \vec{p}_p + \vec{p}_n' = m_p \vec{v}_p + m_n \vec{v}_n'$ and $E_n = E_p + E_n' = mv_p^2/2 + mv_n'^2/2$, if we put $m_n = m_p$ and we suppose that masses are constants, the resulting system of equation is that of a rectangular triangle formed by the velocities of the problem, with \vec{p}_n as the hypotenuse. So, if the energies at play are sufficiently small with respect to the neutron mass, the relation can be used to select elastic events based on the angle between the first proton track, and the segment joining the two vertices of interaction, which is supposed to be the path of the scattered neutron. If this angle (θ_v) is close to 90 degrees (with a chosen confidence interval of $\pm 5^\circ$) the interaction is considered good for reconstruction, if it is not it is discarded by the algorithm. The result is shown in Figure 4.22.

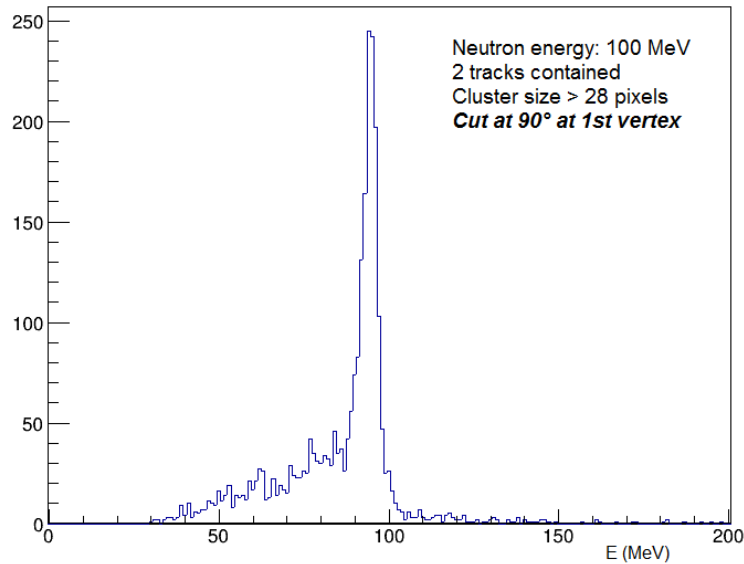


Figure 4.22. Reconstructed neutron energy with the additional constraint on the angle between secondaries at the first vertex $\theta_v \in [85^\circ, 95^\circ]$, using the non-relativistic approximation of elastic scattering with particles of equal mass. The double peak and the background present in Figure 4.21 are both drastically reduced.

As can be seen, the inelastic contribution is practically gone, while DES events have been for the most part spared by the cut, and a single peak is now observed. To further emphasize this point, another plot showing the separate contribution of DES and inelastic events has been made in Figure 4.23. It can be seen that the purely inelastic distribution is reduced to a small background; still, the background is not yet fully removed, and a shoulder of additional contribution is still present. The nature of these events, which are neither double elastic scatterings nor purely inelastic interactions, is still to be determined. One hypothesis is that those are

combination of elastic and inelastic scatterings, more precisely events where the first interaction is elastic, so that the neutron and the proton depart at the correct angle between each other, and the second is inelastic and creates a wrong estimate. A thorough analysis of such events is on the works.

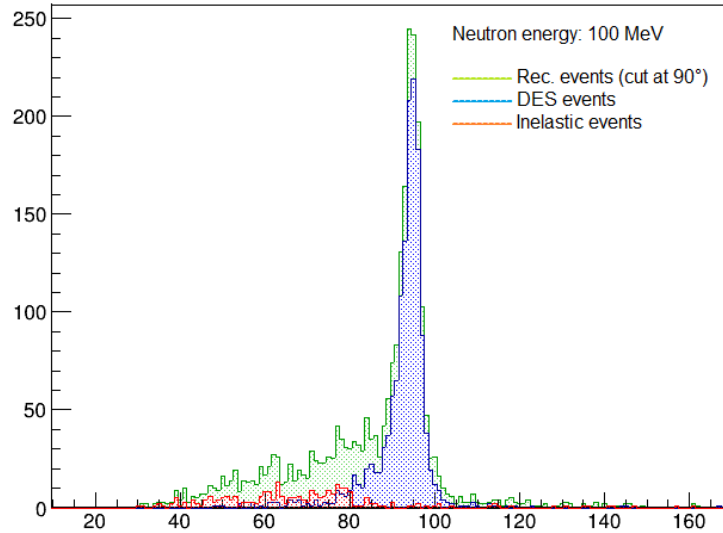


Figure 4.23. Separate contributions to the reconstructed E_n with constraint on θ_v . Almost all the events selected are now DESs (blue), while the purely inelastic contribution (red) is a small flat background. A residual shoulder of not-DES events is still observed at the left of the peak region.

To conclude the discussion on energy, the plot of the two proton energies with the angular cut is indicated in Figure 4.24. The distribution of E reconstructed (the blue curve) resembles more the one obtained with Monte Carlo, even if a slight overpopulation at low values is still present, and more energetic proton tracks are more excluded by the angular cut.

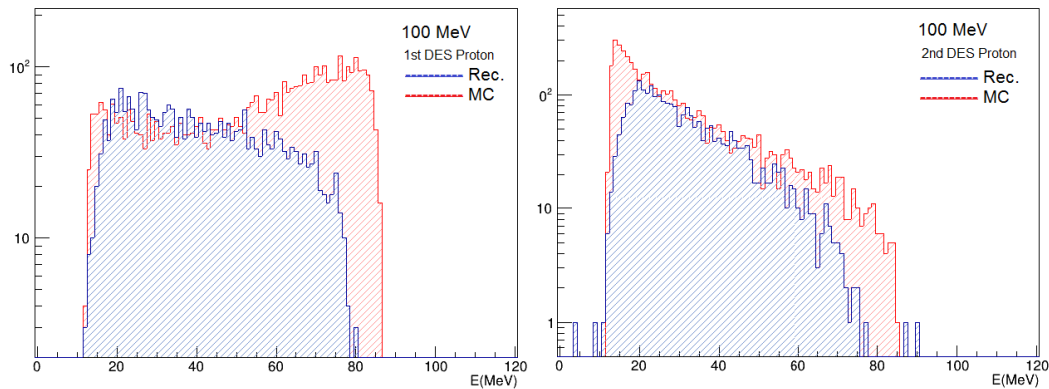


Figure 4.24. Reconstructed (blue) and (red) proton kinetic energies in DES events with angular constraint on θ_v .

4.3.2 Angles

The angle between the neutron entering the tracker and the first scattered proton is obtained through momentum reconstruction, using again Eq. (3.1). The proton and neutron momenta are extracted by inverting Eq. (4.2), so the reconstruction of θ depends from the resolution on the two vertices and also on the computation of E_p . The distributions of θ and θ' reconstructed is presented in Figure 4.25, again with the constraint of having $\theta_v \in [85^\circ, 95^\circ]$. A slight inconsistency with the theory is observed, in that the first proton, being on average more energetic than the second, should be emitted at angles closer to 0° . Instead, θ' appears to have a distribution peaked at smaller angles than θ . The reason for this anomalous behaviour could be once again attributed to mixed elastic-inelastic events, with an SES taking place at the first vertex, and the second vertex being inelastic, thus emitting particles at higher energy than a second elastic scattering in a DES event. Another possibility is that the asymmetric tails in the reconstruction of the direction along the z axis (see Figure 4.13) are responsible for an incorrect angle computation. The most likely hypothesis is that a cumulation of the two distorting effects is observed in the red graph.

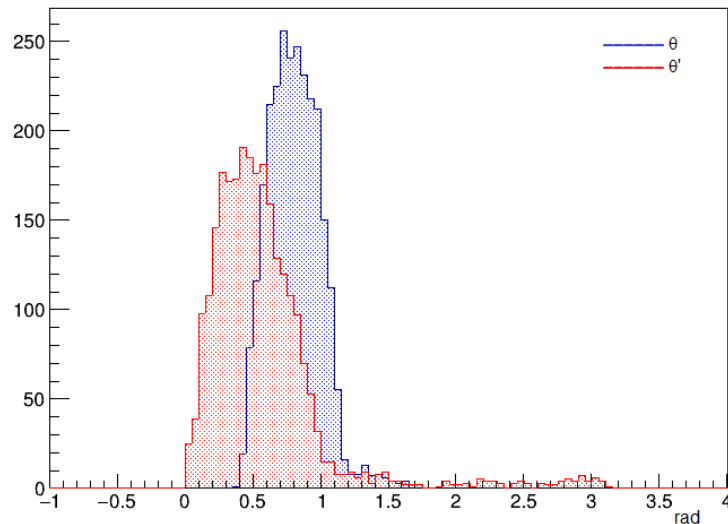


Figure 4.25. Distribution of reconstructed θ (blue) and θ' (red) for $E_n=100$ MeV.

Making the comparison with Monte Carlo data³, the influence of an incorrect evaluation on the direction of z seems to have a solid foundation. As can be seen, the linear correlation is observed, while at the same time a number of angles are reconstructed on another line corresponding to values of $\theta_R = \pi - \theta_{MC}$. The occurrence of this mistake varies with the initial neutron energy, going from about 3% at $E_n = 100$ MeV up to 15% at $E_n = 400$ MeV, where the percentage is out of the total number of tracks in DES candidates events. It is likely that these mistakes are caused by the “reflection” of the z component of the particle direction in space,

³In this case, it means taking the direction of the protons from the simulation. Since information on the neutron direction is not directly saved in the event tree arrays, the vertices are taken from the reconstruction.

due to a wrong computation of the position of the Bragg peak, or to multi-particle clusters being assembled inside a track candidate, and it is thought that angles can be returned to the correct value if a more efficient method of determining the direction is found. It is only for lack of time that this effect has not been fully understood, but progress is expected with further studies.

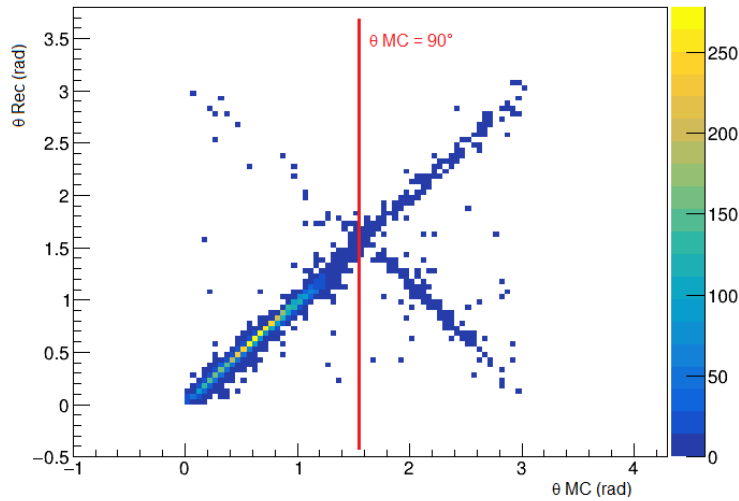


Figure 4.26. Scatter plot of θ reconstructed with the first proton direction taken from MC truth ($E_n = 100$ MeV).

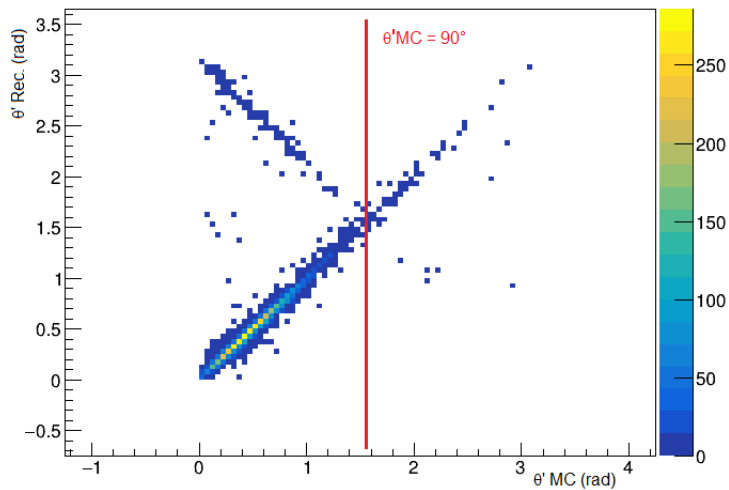


Figure 4.27. Scatter plot of θ' reconstructed with the second proton direction taken from MC truth ($E_n = 100$ MeV).

4.3.3 Backpointing capability

Since one of the aims of MONDO is to have a good backpointing resolution in order to distinguish radiation coming from the patient from that originated through

moderation processes, Eq. (4.1) is used as a method of reconstructing the point of origin of the incoming neutron. The procedure is the following: a line is traced with the direction of \vec{p}_n , the reconstructed neutron momentum, passing through the first vertex of the interaction; a second line is drawn passing through $(0, 0, -20)$, with direction determined by the user; the CPA is computed among the two lines, and if the neutron line of flight goes from its origin to its first interaction vertex, the calculation should give precisely the coordinates of the source. The result for $E_n = 100$ MeV is presented in Figure 4.28. Two lines have been used to determine the point of closest approach, one with versor along x $(1, 0, 0)$, the other along y $(0, 1, 0)$. The distribution of the coordinates deduced with the CPA method with the two lines show clear peaks at the expected point. Depending on along which direction one decides to compute the origin, the spread is larger for the coordinate along which the neutron direction is computed. Further studies on the detector geometry and on the origin of the asymmetry are planned.

4.3.4 Resolution and efficiency plots

The final plots made by the author of this thesis work are estimates on the energy and backpointing resolution, and on efficiency of detection and reconstruction, using the algorithm of DES event candidates selection described in this chapter. For this purpose, simulations at different E_n have been realised, with 3×10^6 neutrons for each energy impacting on the detector, and following the procedure of DES reconstruction illustrated in this chapter. The resulting plots, corresponding to Figures 4.23 and 4.28 in the case of 100 MeV, are fitted with a Gaussian function, of which the value of σ is taken as the useful parameter. The full results can be seen in Appendix A; due to reasons of low statistics (caused mainly by the containment requirement, which limits greatly the number of reconstructable double scattering events above $E_n = 200$ MeV), inefficiency of the method and/or sizable background, only values in the interval 50-200 MeV can be reported. The result for the energy is presented in Figure 4.29 in terms of the percentage relative standard deviation, and it is found to be comprised between 2.5% and 3.5%. The values quoted from [8] for a preliminary energy resolution through reconstructed DES are between 3.5% and 5.5%, so overall the algorithm allows, at least in the case of E_n in the range 50-100 MeV, where little to no background affects the peak formation and the majority of DES events are contained, for a 1% better relative energy resolution.

As far as backpointing is concerned, the preliminary results of [8] with reconstructed DES with Gaussian fits gave an estimate better than 1 cm in the energy range of 50-200 MeV. The result of this work, shown in Figure 4.30, using a line in the x direction for CPA calculation, is consistent with the prediction up until E_n of 100 MeV, after which the resolution worsens. This is expected because of inaccuracies in the direction estimate subject of analysis in the previous sections. Nevertheless the procedure is clear, and the computation of the origin coordinates gives an important result for a preliminary backpointing capability estimate. For the purpose of discriminating background neutrons from those coming from fragmentation, the algorithm is able to make a prediction with $\simeq 1$ cm resolution, which is already very effective and can only be improved by finding the right corrections to the angular reconstruction method.

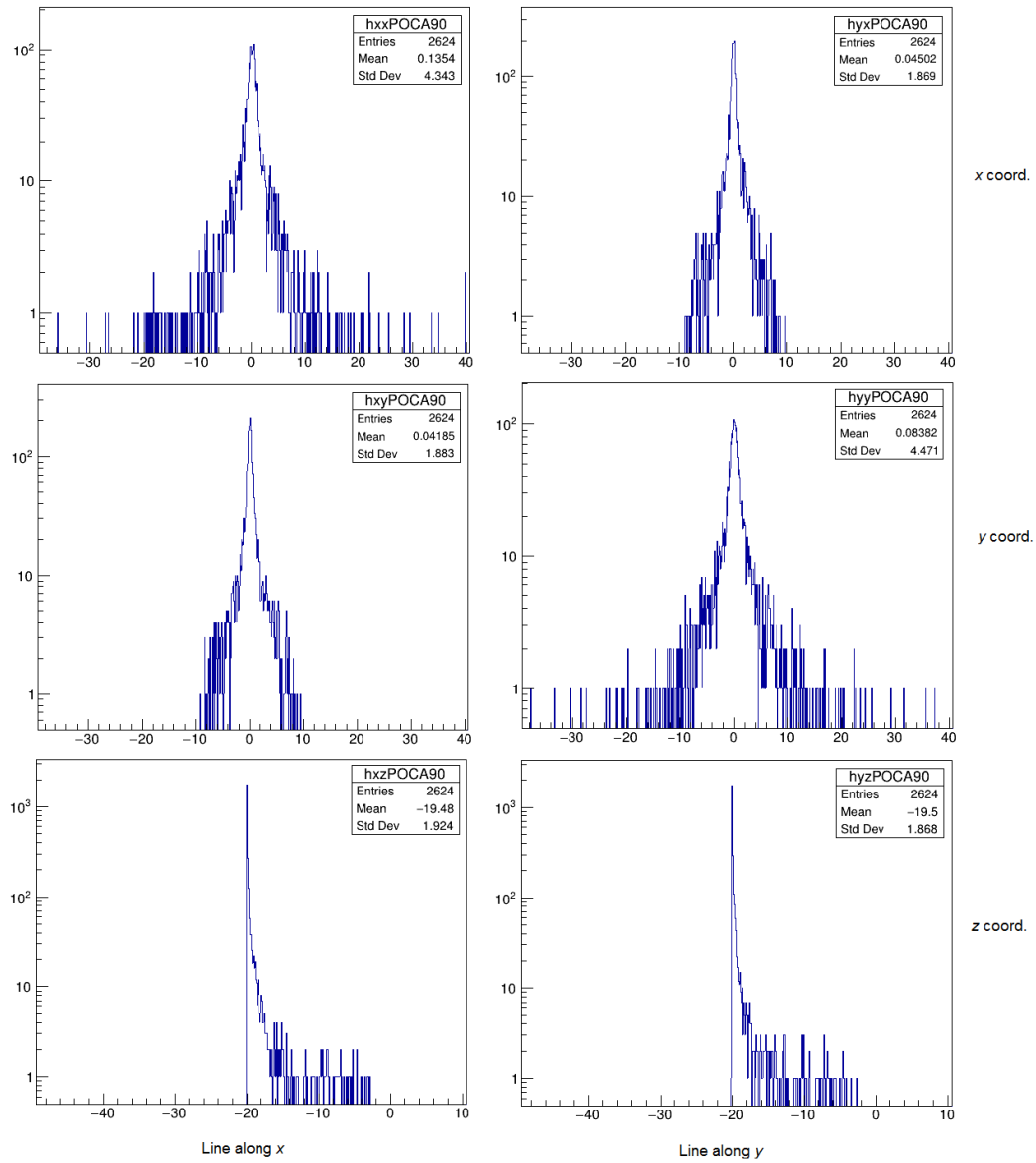


Figure 4.28. Distributions of the neutron origin coordinate estimated through the CPA method for $E_n = 100$ MeV. Depending on the axis chosen for taking the distance with the neutron trajectory, the spread is larger for the coordinate in that direction.

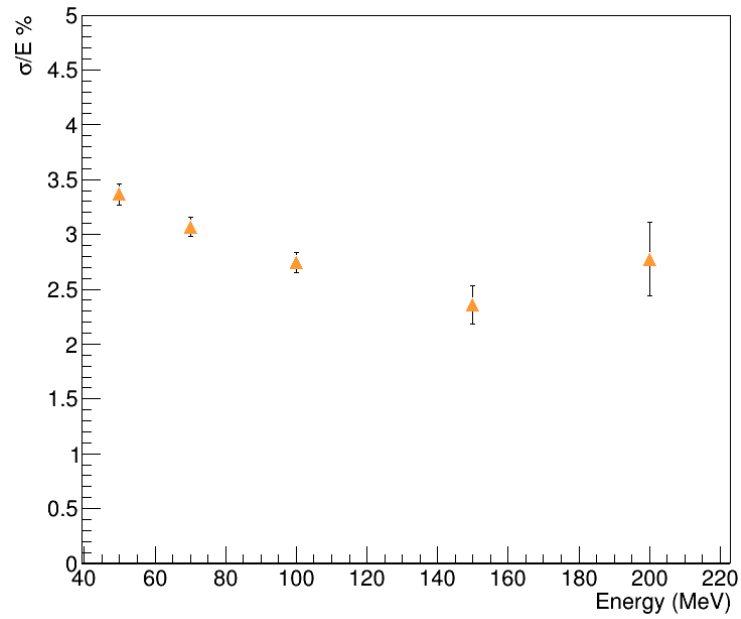


Figure 4.29. Energy resolution taken from Gaussian fit of the reconstructed E_n distribution.

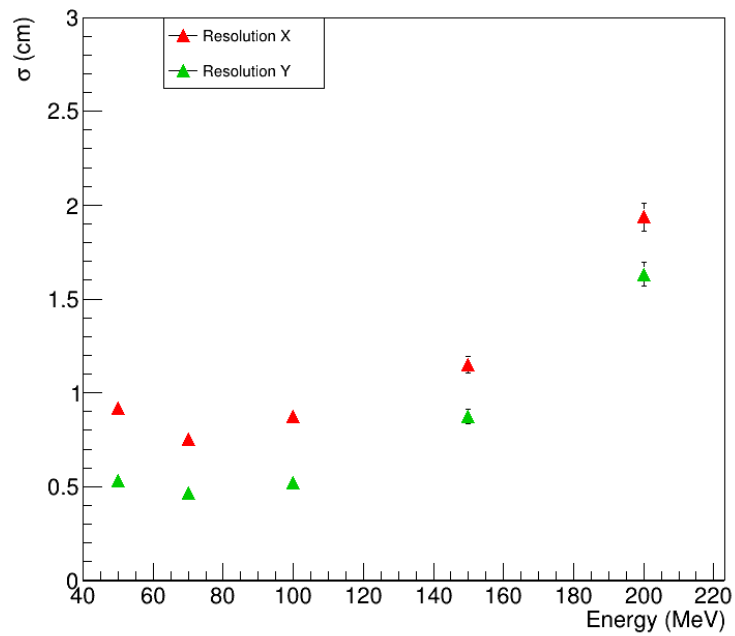


Figure 4.30. Backpointing capability from Gaussian fit of the reconstructed neutron beam starting point.

To give an estimate on the detection efficiency, it is first useful to see the trend at which the rate of reconstructed events evolve as function of the neutron energy. The plot in Figure 4.31 adds to the number of interactions per neutron (squares) the amount of reconstructed events as two contained tracks (triangles) with and without the selection on the angle between secondaries $\theta_v \simeq 90^\circ$. A consideration to be drawn out of this plot is that the constraint on the angle and on the minimum cluster dimension cuts off DES events down to almost two orders of magnitude at E_n below 50 MeV, and about 10 times less at 50 MeV. After 100 MeV, the number of events interpreted as fully contained DES seems to follow closely the number of “detectable” Monte Carlo DES, with the same constraints as those for the hardware, so the percentage of selected events out of the total seems to remain constant. This is confirmed by making the ratio between the two populations (reconstructed with angular cut and MC double elastic scatterings); this reconstruction efficiency reaches a *plateau* at 70% for energies above 100 MeV.

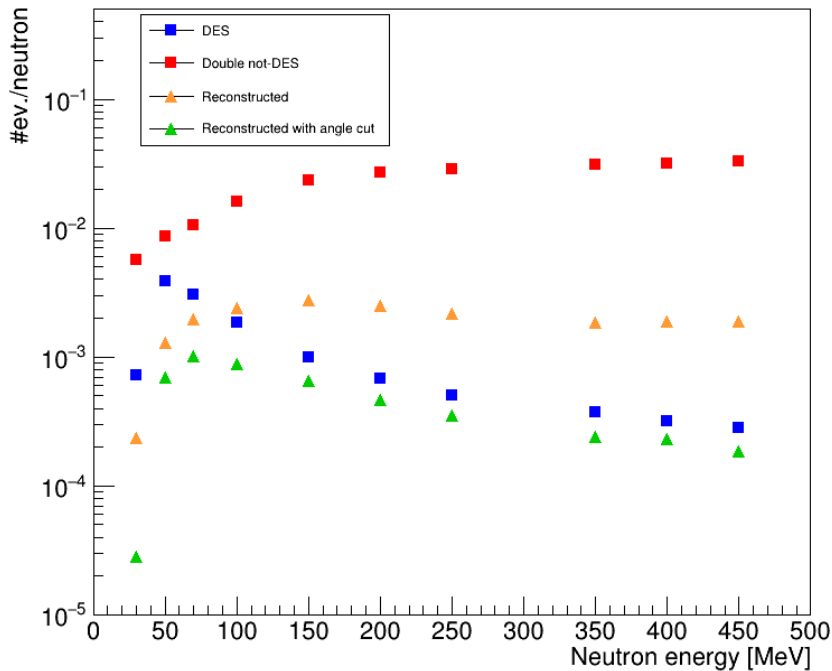


Figure 4.31. Rate of double-track contained events as function of E_n . Both DES and not-DES events are considered with two particles with MC range > 2 mm. The rate of general reconstructed events (orange) are clearly subject to a sizable contamination of not-DES events, dominant at high energies. Putting the constraint at the angle on the first vertex of interaction, the rate (green) remains under the DES population.

The selection efficiency computed as the ratio between the number of events that are really DES by Monte Carlo truth out of all those estimated to be good for the neutron four-momentum characterisation (the orange triangles) is shown in Figure 4.32 (Right). The low values at $E_n = 30$ MeV and $E_n \geq 350$ MeV are mainly due to the very low statistics on DES events, since at low energies the limit on cluster size kills off the majority of elastic proton tracks, and leaves only the more energetic inelastic interactions, and after 250 MeV the containment requirement is

the most limiting factor, in which case very few DES events are fully contained and reconstructed events are mostly due to the constant background of inelastic and mixed interactions. It can be concluded that selection is very effective at energies of 50-70 MeV, as it can be deduced also by looking at the sharp peaks obtained in the energy, and it can be improved by increasing the statistics and moving beyond the containment limit by measuring the proton energies by means of the Bethe equation (Eq. (1.1)).

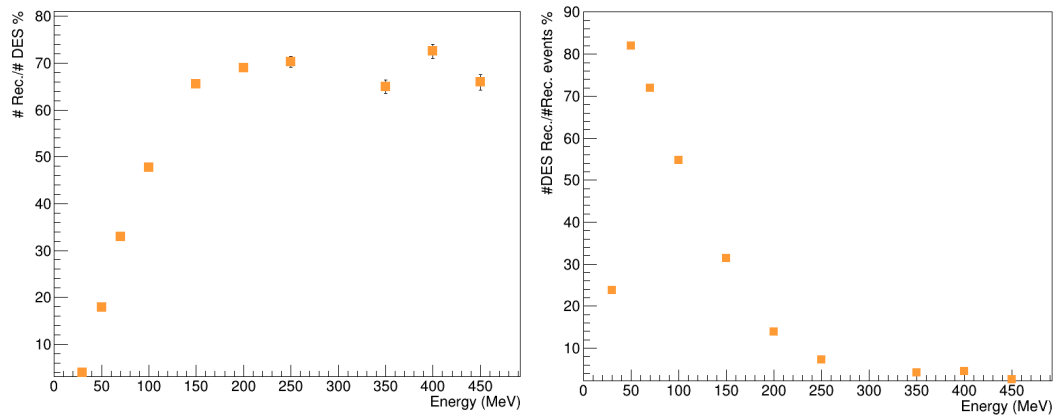


Figure 4.32. Reconstruction (Left) and selection (Right) efficiencies estimates. The error bars correspond to the purely statistical contribution.

Conclusions

This thesis work has illustrated the need for a secondary neutron tracker in Particle Therapy, an innovative treatment for cancer pathologies, taking advantage of the dose distribution in matter of charged particles like protons and heavy ions, which allows to focus the damaging effect of radiation on the tumour zone and spare nearby sane tissues. The efficacy of PT is limited by the phenomenon of nuclear fragmentation, consisting on the production of numerous neutral and charged secondaries through strong interactions of the therapeutic beam with the human body.

Additional dose induced by fast and ultra-fast neutrons, in particular, is considered the most abundant and dangerous unwanted contribution released on healthy organs, both in- and out-of-field, and a likely candidate for the insurgence of long term complications like Secondary Malignant Neoplasms. The main aim of the MONDO project is the development of a tracker able to fully characterise this secondary neutron component in the energy range of 10-400 MeV in order to improve their modelling inside treatment planning system for PT.

The detector strategy is based on the detection of double elastic scattering events in the tracker scintillating fibers, and the detection of light produced by the recoiling protons with a very high granularity, thus reconstructing both energy and direction with great precision. Simulations with Monte Carlo methods based on the FLUKA code are used to optimize the tracker geometry and reconstruction method, and study the expected performances on response, efficiency and resolution. The latest results also include the sensor architecture and technical properties.

During my thesis I developed an algorithm for event reconstruction based on measurable data coming from the hardware component of the detector, taking advantage of the fact that they have been fully integrated in the FLUKA simulation and their performances is now part of the accessible MC information. It is able to select interesting events by means of a three-dimensional track building technique and compute the expected number of double elastic interactions and background due to inelastic scatterings as function of the initial kinetic energy. The results are in good agreement with previous studies, and the algorithm selects DES events with efficiency of 70%. A method of selection is already working at energies below 200 MeV, giving an achievable energy resolution of about 3-4% for contained events. Backpointing capability has also been evaluated, giving an estimated resolution < 2 cm.

More improvement is expected on direction reconstruction and detection efficiency, moving beyond the containment restriction and computing the energy by means of the average dE/dx following the Bethe-Bloch equation, considerably increasing the statistics on DES events. Other improvements will include exploiting the timing

information of the pixels to determine the chronological order of the tracks and the possibility to study in detail the topological features of inelastic tracks through a versatile function of event display. Further studies will also investigate new methods of selection taking into account the mixed elastic-inelastic interactions and start working beyond the monochromatic neutron beam configuration, getting closer to a real therapy situation.

Appendix A

This appendix includes all the distributions of neutron energy and CPA that have been obtained with E_n going from 30 MeV to 400 MeV. The Gaussian fits used to evaluate the resolution are also reported with the computed parameters. The constraints used for the reconstruction are summarised here:

- track candidates are made out of two clusters, one on view x and one on view y, both with number of pixels > 28 , mirroring the requirement of a proton range of about 2 mm in MONDO;
- the event has two and only two track candidates, one for each proton in a double scattering;
- both tracks are fully contained inside the confidence volume of MONDO (see Section 4.2);
- to select double elastic scatterings, a constraint is imposed on the angle between the first recoil proton and the scattered neutron, which based on kinematics of elastic scattering in the non-relativistic regime, is 90° (see Section 4.3).

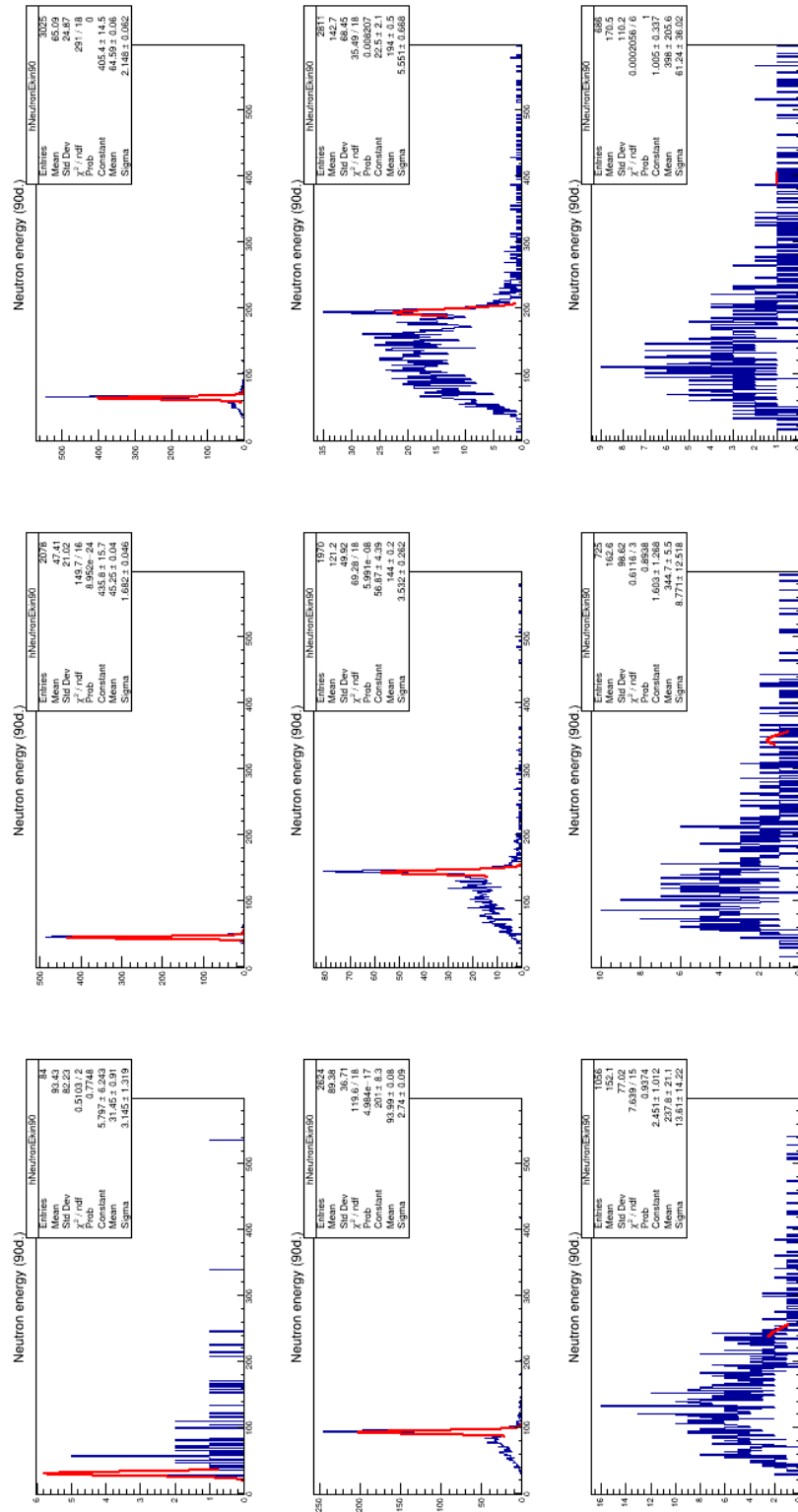
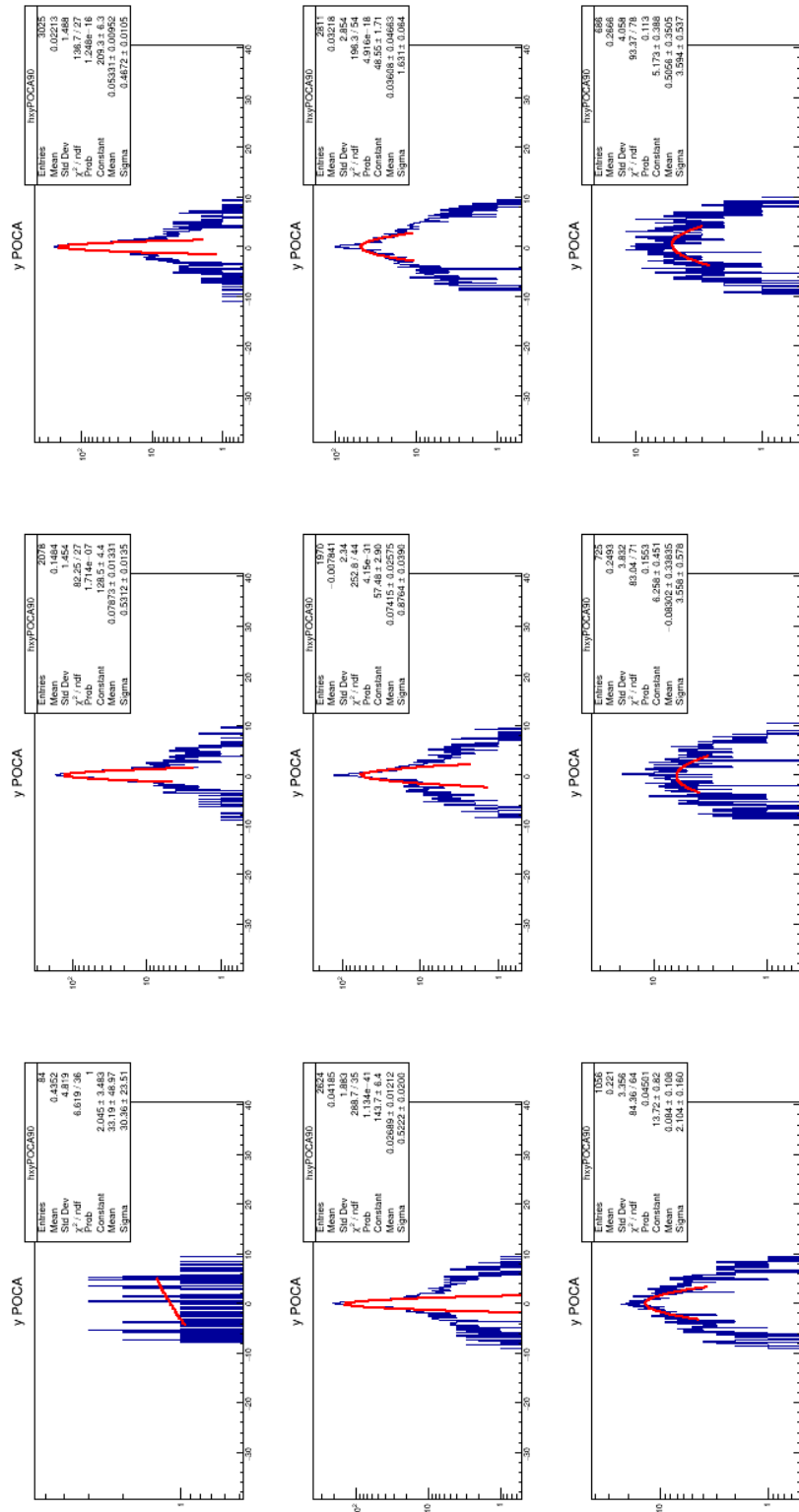


Figure 4.33. Neutron energies reconstructed.

Figure 4.35. y coordinate of CPA.

Bibliography

- [1] G. Battistoni et al. “Overview of the FLUKA code”. In: *Annals of Nuclear Energy* 82 (2015), pp. 10–18. DOI: 10.1016/j.anucene.2014.11.007.
- [2] B. Bednarz, X. G. Xu, and H. Paganetti. “A review of dosimetry studies on external-beam radiation treatment with respect to second cancer induction”. In: *Physics in Medicine and Biology* 53 (2008), pp. 193–241.
- [3] T. Bortfeld and W. Schlegel. “An analytical approximation of depth - dose distributions for therapeutic proton beams”. In: *Phys. Med. Biol.* 41 (1996), pp. 1331–1339.
- [4] R. L. Bramblett, R. I. Ewing, and T. W. Bonner. “A New Type of Neutron Spectrometer”. In: *Nucl. Instrum. Meth.* 9 (1960), p. 1.
- [5] P. R. P. Coelho, A. A. Da Silva, and J. R. Maiorino. “Neutron Energy Spectrum Measurements of Neutron Sources with an NE-213 Spectrometer”. In: *Nucl. Instrum. Meth. A* 280 (1989), p. 270.
- [6] E. U. Condon and G. Breit. “The Energy Distribution of Neutrons Slowed by Elastic Impacts”. In: *Phys. Rev.* 49 (1936), p. 229.
- [7] V. Giacometti et al. “Characterisation of the MONDO detector response to neutrons by means of a FLUKA Monte Carlo simulation”. In: *Radiation Measurements* 119 (2018), pp. 144–149. DOI: 10.1016/j.radmeas.2018.10.006.
- [8] E. Gioscio, G. Battistoni, A. Bochetti, et al. “Development of a novel neutron tracker for the characterisation of secondary neutrons emitted in Particle Therapy”. In: *Nuclear Inst. and Methods in Physics Research, A* 162862 (2019). DOI: 10.1016/j.nima.2019.162862.
- [9] S. Gunzert-Marx et al. “Secondary beam fragments produced by 200 MeV/u ^{12}C ions in water and their dose contributions in carbon ion radiotherapy”. In: *New Journal of Physics* 10 (2008). DOI: 10.1088/1367-2630/10/7/075003.
- [10] S. Gunzert-Marx, D. Schardt, and R. S. Simon. “Fast neutrons produced by nuclear fragmentation in treatment irradiations with ^{12}C beam”. In: *Radiat. Protect. Dosim.* 110 (1-4) (2004), pp. 595–600. DOI: 10.1093/rpd/nch138.
- [11] E. J. Hall. *Radiobiology for the radiologist*. Philadelphia: Lippincott Williams & Wilkins, 2000.
- [12] ICRP. “Recommendations of the International Commission on Radiological Protection”. In: *ICRP Publication* 103 (2007).

- [13] G. F. Knoll. *Radiation Detection and Measurement, Third Edition*. New York: John Wiley & Sons, Inc., 2000.
- [14] H. Koshiishi et al. "Evaluation of the neutron radiation environment inside the international space station based on the Bonner ball neutron detector experiment". In: *Radiation Measurements* 42(9) (2007), pp. 1510–1520.
- [15] Kuraray, ed. *Plastic Scintillating Fibers*. 2014. URL: <https://www.kuraray.com>.
- [16] C. La Tessa et al. "Characterization of the secondary neutron yield produced during treatment of an anthropomorphic phantom with x-rays, protons and carbon ions". In: *Physics in Medicine and Biology* 59 (2014), p. 2111.
- [17] W. R. Leo. *Techniques for Nuclear and Particle Physics Experiments*. Berlin, Heidelberg: Springer-Verlag, 1987.
- [18] M. Marafini et al. "MONDO: a neutron tracker for particle therapy secondary emission characterization". In: *Physics in Medicine and Biology* 62 (2017), pp. 3299–3312. DOI: 10.1088/1361-6560/aa623a.
- [19] D. K. Meyers. *Low Level Radiation: A Review of Current Estimates of Hazards to Human Populations*. Report AECL 5715. Atomic Energy of Canada, Ltd., 1982.
- [20] R. Mirabelli. "Development of a new tracking device for characterization and monitoring of ultra fast neutron beams". Ph.D. Thesis. Università di Roma "La Sapienza", 2019.
- [21] R. Mirabelli et al. "The MONDO detector prototype development and test: steps towards a SPAD-CMOS based integrated readout (SBAM sensor)". In: *IEEE Trans. Nucl. Sci.* 65 (2) (2017), pp. 744–751. DOI: 10.1109/TNS.2017.2785768.
- [22] W. Newhauser and M. Durante. "Assessing the risk of second malignancies after modern radiotherapy". In: *Nat. Rev. Cancer* 11 (2011), p. 438.
- [23] Saint-Gobain, ed. *Plastic Scintillating Fibers*. 2019. URL: <https://www.crystals.saint-gobain.com>.
- [24] U. Schneider et al. "Secondary neutron dose during proton therapy using spot scanning". In: *Int. J. Radiat. Oncol. Biol. Phys.* 53 (2002), pp. 244–251. DOI: 10.1016/S0360-3016(01)02826-7.
- [25] R. Takam et al. "Out-of-Field Neutron and Leakage Photon Exposures and the Associated Risk of Second Cancers in High-Energy Photon Radiotherapy: Current Status". In: *Radiation research* 176 (2011), pp. 508–20. DOI: 10.2307/41318216.
- [26] M. Tanabashi et al. "Review of Particle Physics". In: *Phys. Rev. D* 98, 030001 (2018). Ed. by Particle Data Group. DOI: 10.1103/PhysRevD.98.030001.
- [27] F. Tommasino, E. Scifoni, and M. Durante. "New ions for therapy". In: *Int. J. Particle Ther.* 2 (3) (2015), pp. 428–438. DOI: 10.14338/IJPT-15-00027.1.
- [28] S. M. Valle et al. "The MONDO project: A secondary neutron tracker detector for particle therapy". In: *Nuclear Instruments and Methods in Physics Research A* 845 (2017), pp. 556–559. DOI: 10.1016/j.nima.2016.05.001.

- [29] R. Wilson. “Radiological use of fast protons”. In: *Radiology* 47 (1946), pp. 487–491.